

1 **Characteristics of airborne black carbon-containing particles**
2 **during the 2021 summer COVID-19 lockdown in a typical**
3 **Yangtze River Delta city, China**

4
5 Yuan Dai^{1,2,3}, Junfeng Wang^{1,2}, Houjun Wang³, Shijie Cui^{1,2}, Yunjiang Zhang^{1,2},
6 Haiwei Li^{1,2}, Yun Wu^{1,2}, Ming Wang^{1,2}, Eleonora Aruffo⁵, Xinlei Ge^{1,2,4*}

7
8 ¹Jiangsu Key Laboratory of Atmospheric Environment Monitoring and Pollution
9 Control, Collaborative Innovation Center of Atmospheric Environment and Equipment
10 Technology, School of Environmental Science and Engineering, Nanjing University of
11 Information Science and Technology, Nanjing 210044, China

12 ²International Joint Laboratory on Climate and Environment Change (ILCEC), Nanjing
13 University of Information Science and Technology, 210044 Nanjing, China

14 ³Yangzhou Environmental Monitoring Center, Yangzhou 225009, China

15 ⁴School of Environment and Energy Engineering, Anhui Jianzhu University, Hefei
16 230601, China

17 ⁵Department of Advanced Technologies in Medicine & Dentistry, University “G.
18 d’Annunzio” of Chieti-Pescara; Center for Advanced Studies and Technology-CAST,
19 Chieti 66100, Italy

20
21 **Correspondence:** Xinlei Ge (caxinra@163.com)

带格式的: 行距: 单倍行距

设置了格式: 字体颜色: 自动设置

设置了格式: 字体颜色: 自动设置

带格式的: 左

22 **Abstract**

23 Black carbon-containing particles (BCc) are ubiquitous in ambient air, significantly
24 contributing to particulate matter (PM) pollution. The unexpected outbreak of the
25 COVID-19 pandemic in the summer of 2021 prompted a localized and prolonged
26 lockdown in Yangzhou City, situated in the Yangtze River Delta, China. This lockdown
27 led to, significantly altering in local anthropogenic emissions, while neighboring cities
28 continued regular operations, providing a unique opportunity for the investigation of
29 BCc characteristics ~~affected~~ influenced by varying different emission conditions.
30 Single particle aerosol mass spectrometer (SPA-MS) analysis revealed a notable
31 decrease in the proportion of freshly emitted BCc during the lockdown period (LD_c).
32 However, we did observe a concurrent 7% increase in PM_{2.5} concentration of during
33 LD, with a higher proportion of aged BCc₇ compared to the period before the lockdown
34 (BLD). Evidence shows that regional transportation plays a vital role in the
35 enhancement of PM_{2.5} during LD. Moreover, reactive trace gases (e.g., NO_x, SO₂, and
36 VOCs) could form thick coatings on pre-existing particles likely via enhanced
37 heterogeneous hydrolysis under high RH as well, resulting in significant BCc particle
38 growth (~600 nm), as well as PM_{2.5}, during LD. ~~Furthermore, BCc source~~
39 ~~apportionment reveals that BCc particles were primarily of local origin (78%) in~~
40 ~~Yangzhou during normal summertime. However, coal combustion (23%) and vehicle~~
41 ~~emissions (21%) were prominent non-local pollution sources, with the air mass~~
42 ~~originating from the southeast, along with biomass burning emissions (19%) from the~~
43 ~~northeast, contributing significantly.~~ Our study highlights that short-term, strict local
44 emission controls may not effectively reduce PM pollution due to the complex
45 production and transmission characteristics of BCc and the non-linear responses of
46 PM_{2.5} to its precursors. Achieving further effective PM_{2.5} reduction mandates a focus
47 on nuanced control of BCc and necessitates a comprehensive and extensive approach
48 with a regionally coordinated and balanced control strategy through joint regulation.

- 设置了格式: 突出显示
- 设置了格式: 字体: 非倾斜, 突出显示
- 设置了格式: 突出显示
- 设置了格式: 字体: 非倾斜, 突出显示
- 设置了格式: 字体: 非倾斜, 突出显示
- 设置了格式: 突出显示
- 设置了格式: 字体: 非倾斜, 突出显示
- 设置了格式: 突出显示
- 设置了格式: 字体: 非倾斜, 突出显示
- 设置了格式: 字体: 非倾斜, 突出显示
- 设置了格式: 突出显示
- 设置了格式: 字体: 非倾斜, 突出显示
- 设置了格式: 突出显示
- 设置了格式: 字体: 非倾斜, 突出显示
- 设置了格式: 突出显示
- 设置了格式: 字体: 非倾斜, 突出显示
- 设置了格式: 突出显示
- 设置了格式: 字体: 非倾斜, 突出显示
- 设置了格式: 突出显示
- 设置了格式: 字体: 非倾斜, 突出显示
- 设置了格式: 突出显示
- 设置了格式: 字体: 非倾斜
- 设置了格式: 突出显示
- 设置了格式: 下标, 突出显示
- 设置了格式: 突出显示
- 设置了格式: 下标, 突出显示
- 设置了格式: 突出显示

49

50 **2.1. Introduction**

51 China has implemented long-term clean air measures to cut down anthropogenic
52 emissions and improve air quality (Ge et al., 2020), resulting in a nationwide reduction
53 of average fine particulate matter (PM_{2.5}, aerodynamic diameter < 2.5 μm) level from
54 50 μg m⁻³ in 2015 to 30 μg m⁻³ in 2020 (Zhou et al., 2022). However, this PM_{2.5}
55 concentration remains significantly higher than the new World Health Organization
56 (WHO) guideline value of 5 μg m⁻³ (WHO Global Air Quality Guidelines, 2021).

57

58 Black carbon (BC) is a ubiquitous component of aerosols, typically constituting a small
59 proportion (5~10%) of PM_{2.5} in the atmosphere (Chen et al., 2020). However, freshly
60 emitted BC evolves into BC-containing particles (BCc) by undergoing atmospheric
61 aging, contributing to a rise in the total mass of PM_{2.5} through processes of coating or
62 embedding by other materials (Bond and Bergstrom, 2006; Peng et al., 2016). The
63 number and mass fraction of BCc can exceed 60% and 50% of PM_{2.5}, respectively,
64 emphasizing the significant role of BC in elevating the mass concentration of
65 particulate matter (PM) (Sun et al., 2022; Xie et al., 2020; Chen et al., 2020).

66

67

68 ~~China has implemented long-term clean air measures to cut down anthropogenic~~
69 ~~emissions and improve air quality (Ge et al., 2020), resulting in a nationwide reduction~~
70 ~~of average fine particulate matter (PM_{2.5}, aerodynamic diameter < 2.5 μm) level from~~
71 ~~50 μg m⁻³ in 2015 to 30 μg m⁻³ in 2020 (Zhou et al., 2022). However, this PM_{2.5}~~
72 ~~concentration remains significantly higher than the new World Health Organization~~
73 ~~(WHO) guideline value of 5 μg m⁻³ (WHO global air quality guidelines, 2021). Black~~
74 ~~carbon (BC) is a ubiquitous component of PM_{2.5} that can mix with various species,~~
75 ~~and the number fraction of BC-containing particles (BCc) can be higher than 50% of~~
76 ~~PM_{2.5} in China (Sun et al., 2022; Xie et al., 2020; Chen et al., 2020). Additionally, t~~

77 The atmospheric aging of BCc involves intricate chemical and physical transformations
78 that influence their mixing state, morphology, hygroscopicity, and optical properties,

79 all of which have profound implications for climate and human health (Bond et al.,
80 2013; Ramanathan and Carmichael et al., 2008)he atmospheric aging of BCc involves

81 complex chemical and physical processes, influencing their mixing state, morphology,
82 hygroscopic and optical properties, etc., ultimately impacting their climatic and health

83 effects (Bond et al., 2013; Ramanathan et al., 2008). Reducing the mass loading of BCc
84 is therefore essential to comply with the new WHO PM_{2.5} guideline. For example,

85 freshly emitted BC particles are initially hydrophobic but possess a porous surface
86 structure that facilitates the internal or external mixing with co-emitted primary

87 organic/inorganic and secondary materials that are associated with BCfreshly emitted
88 BC particles are initially hydrophobic but possess a porous surface structure that

89 facilitates the adsorption and condensation of coating materials to form irregular

设置了格式: 突出显示

设置了格式: 突出显示

90 aggregates, such as secondary organic and inorganic salts (Cheng et al., 2012; J-Li et
91 al., 2020). On the other hand, BCc undergoes variable continually aging processes,
92 including encompassing the condensation of low-volatility vapors (Li et al., 2022),
93 coagulation with preexisting aerosols (Kondo et al., 2011), and heterogeneous oxidation
94 with gaseous pollutants (Zhang et al., 2024). This alteration may affect the coating
95 thickness, morphology, size distribution, and hygroscopicity of BCc, thereby impacting
96 their climate forcing as well as atmospheric lifetime thereby impacting their wet optical
97 and radiative properties, deposition efficiency and hence atmospheric lifetime (Luo et
98 al., 2022; Taylor et al., 2014). High loading of atmospheric BCc could also depress the
99 development of the planetary boundary layer and exacerbate PM pollution episodes
100 (Huang et al., 2018). In dynamic atmospheric environments, BCc characteristics are
101 influenced by various combustion sources and emission conditions, including local
102 industrial burning, vehicle exhausts, residential coal burning, and biomass burning (J-
103 Li et al., 2020; Sedlacek et al., 2022; Zhang et al., 2018), as well as long-range transport
104 from other regions (Adachi et al., 2014; J-Zhang et al., 2021). Characteristics of freshly
105 emitted BC can be influenced by combustion source and emission conditions. Those
106 diverse wide variety of conditions complicate the development of parameterizations of
107 BCc properties. Moreover, the insufficient understanding of complex emission sources,
108 aging processes, and physical properties of BCc, hampering the effectiveness of air
109 quality remediation (Cappa et al., 2019; Kahnert, 2010; Sun et al., 2021).

111 Studies on the effects of large-scale and short-term stringent emission control events on
112 air quality in China have been widely deployed, e.g., the 2008 Beijing Olympic Games
113 (Wang et al., 2010; Zhou et al., 2010), the 2015 Asia-Pacific Economic Cooperation
114 (APEC) (Zhu et al., 2015), the 2014 Nanjing Youth Olympic Games (Wang et al., 2022)
115 and the national COVID-19 lockdown in 2020 winter (Huang et al., 2021; Le et al.,
116 2020; L. Li et al., 2020; Wang et al., 2020) (Huang et al., 2021; Le et al., 2020; Li et al.,
117 2020; Wang et al., 2020). Previous studies extensively investigated air pollutant
118 variations during the COVID-19 lockdown in the winter of 2020 across different
119 regions of the world. Stringent restrictions on industrial and vehicular activities have
120 resulted in significant reductions in gaseous pollutants and particulate matter, not only
121 in megacities (Chen et al., 2020; Jeong et al., 2022; Sun et al., 2020) (Chen et al., 2020;
122 Jeong et al., 2022; Sun et al., 2020) but also in middle-sized cities (Clemente et al.,
123 2022; Wang et al., 2021; Xu et al., 2020) (Clemente et al., 2022; Wang et al., 2021; Xu
124 et al., 2020) and rural areas (Cui et al., 2021, 2020; Jain et al., 2021). Compared to the
125 decreasing trends observed in most cities worldwide, the level of PM_{2.5} in Shanghai
126 (Chang et al., 2020), Hohhot (Zhou et al., 2022), and the Northeast of China Plain (Nie
127 et al., 2021) increased unexpectedly. These observations reveal the complex aerosol
128 chemistry of PM_{2.5} comprising primary and secondary components. The reduction of
129 primary pollutants during lockdown resulted in a shift towards a higher proportion of
130 secondary aerosols, including inorganic and organic species, exhibiting a non-linear
131 response to emission changes (Zhang et al., 2021). Furthermore, some studies

设置了格式: 突出显示

设置了格式: 突出显示

设置了格式: 突出显示

设置了格式: 突出显示

设置了格式: 突出显示

设置了格式: 突出显示

设置了格式: 突出显示

设置了格式: 突出显示

设置了格式: 突出显示

设置了格式: 突出显示

设置了格式: 突出显示

设置了格式: 突出显示

设置了格式: 突出显示

设置了格式: 突出显示

设置了格式: 突出显示

设置了格式: 突出显示

域代码已更改

域代码已更改

域代码已更改

域代码已更改

域代码已更改

域代码已更改

域代码已更改

域代码已更改

域代码已更改

域代码已更改

域代码已更改

域代码已更改

域代码已更改

域代码已更改

域代码已更改

域代码已更改

域代码已更改

域代码已更改

域代码已更改

域代码已更改

域代码已更改

域代码已更改

域代码已更改

域代码已更改

域代码已更改

域代码已更改

132 suggested that the increase in secondary aerosols during lockdown is due to the
133 enhanced atmospheric oxidative capacity resulting from the rise in ozone levels (Y.
134 Wang et al., 2021)(Wang et al., 2021), unfavorable meteorological conditions (Chien et
135 al., 2022; Sulaymon et al., 2021a), changes of local and regional emission sources (Feng
136 et al., 2022). However, most previous studies focused on lockdown events during the
137 cold seasons, and studies on summer lockdown events in China were very limited.

138
139 Yangzhou is located in the central region of the Yangtze River Delta (YRD), at the
140 junction of the Yangtze River and, the Beijing-Hangzhou Grand Canal, which serves as
141 a prominent economic city, industrial-intensive area, and highly active inland shipping
142 node in East China. Due to the complex emissions and feedback with the East Asian
143 monsoons (Ding et al., 2019), this region is susceptible to anthropogenic aerosols,
144 especially BCc originating from chemical, steelmaking, coal-fired, petrochemical
145 enterprises, and transportation, etc. Extensive studies have investigated the responses
146 of atmospheric pollutants to emission changes during the COVID-19 lockdown
147 measures in the YRD (Chen et al., 2021; L.-Li et al., 2020; Qin et al., 2021; K.-Zhang
148 et al., 2022)(Chen et al., 2021; Li et al., 2020; Qin et al., 2021; K. Zhang et al., 2022).
149 However, the key chemical and physical processes specifically responsible for the BCc
150 in this region are still unclear. During the summer of 2021, Yangzhou experienced a
151 resurgence of COVID-19 with over 500 confirmed cases. In response, stringent public
152 health measures were imposed from July 28th to September 10th, including the closure
153 of public transport, and suspension of non-essential industrial plants, restaurants,
154 shopping malls, and entertainment clubs. People were also mandated to quarantine at
155 home. Unlike the nationwide COVID-19 lockdown in China during the cold season of
156 2020 (Le et al., 2020; Sulaymon et al., 2021b), the summer lockdown in Yangzhou was
157 more localized but protracted, significantly altering local anthropogenic emissions
158 while neighboring cities maintained regular operations, which provides a unique
159 opportunity to explore and compare the diverse mixing states and, the aging process of
160 BCc in different anthropogenic emission conditions in summer, investigate the regional
161 transportation of air pollutants in YRD, enhance our knowledge about the formation of
162 BC-associated secondary components (Lei et al., 2021; Zhang et al., 2020) and
163 understand emissions-meteorology interactions (Jiang et al., 2021; Le et al., 2020) in
164 the YRD.

165
166
167
168 Here we report the chemical compositions and aging characteristics of airborne BCc in
169 YRD. Our investigation involved a combination of ground measurements, spaceborne
170 observations, and mass spectrometric analysis conducted during the COVID-19
171 lockdown in the summer of 2021 in Yangzhou. Additionally, We conducted ground
172 measurements, spaceborne observations, and mass spectrometric analysis during the
173 COVID-19 lockdown in the summer of 2021, in Yangzhou. We we employed potential

设置了格式: 突出显示

设置了格式: 突出显示

设置了格式: 突出显示

域代码已更改

设置了格式: 突出显示

174 source contribution function (PSCF) analysis ~~and a novel approach for distinguishing~~
175 ~~local sources_~~ to investigate the air pollution ~~patterns~~ affected by regional transport in
176 the YRD. ~~This study investigated the impact of small scale and short term stringent~~
177 ~~emission controls on local ambient aerosol and the mixing state of BCE, providing~~
178 ~~valuable insights for future air pollution control measures.~~

180 **3.2. Methods**

181 **3.2.1 Sampling site and instruments**

182 The in-situ online measurements were conducted at a rooftop laboratory 20 m above
183 ground located in a national air quality monitoring station, Yangzhou Environmental
184 Monitoring Center (32.41°N, 119.40°E), Yangzhou, China (**Figure 1**). This sampling
185 site is a typical urban site surrounded by residential areas, arterial roads, parks,
186 restaurants, and shopping centers. In this study, the measurement period was divided
187 into three phases: the before-lockdown period (BLD: 30 June to 27 July 2021), the
188 lockdown period (LD: 28 July to 9 September 2021), and the after-lockdown period
189 (ALD: 10 September to 7 October 2021) (**Figure 2**).

190
191 A single-particle aerosol mass spectrometer (SPA-MS, Hexin Analytical Instrument Co.,
192 Ltd., China) was deployed during the field campaign to obtain the chemical
193 composition, size distribution, and mixing state of individual PM_{2.5} particles. **A cyclone**
194 **with a 2.5 μm cutpoint (Model URG-2000-30ED) and a Nafion dryer is equipped in**
195 **front of the sampling inlet. Individual particles are introduced into the SPA-MS through**
196 **a critical orifice at a flow rate of 3 L min⁻¹. A cyclone with 2.5 μm cutpoint (Model**
197 **URG 2000 30ED) and a Nafion dryer are equipped in front of the sampling inlet.**
198 **Individual particles are introduced into the SPA-MS through a critical orifice at a flow**
199 **rate of 3 L min⁻¹.** The vacuum aerodynamic diameters (D_{va}) are determined using the
200 velocities derived from two continuous laser beams (diode Nd: YAG, 532 nm) spaced
201 6 cm apart. Subsequently, these particles are desorbed and ionized by a downstream
202 pulsed laser (266 nm), and ion fragments are generated and measured by a Z-shaped
203 bipolar time-of-flight mass spectrometer. A more detailed description of SPA-MS can
204 be found in previous studies (Li et al., 2011).

205
206 PM_{2.5} mass concentration was measured by a particulate matter monitor (XHPM2000E,
207 Xianhe, China). Nitrogen oxides (NO_x = NO + NO₂), SO₂, and ozone (O₃)
208 concentrations were detected with a set of Thermo Fisher Scientific instruments
209 (Models 42i, 43i, and 49i). The concentrations of 103 volatile organic compounds
210 (VOCs) in ambient air, comprising 57 ozone precursors (PAMS), 12 aldehydes and
211 ketones, and 34 toxic organics (TO15), were continuously monitored at hourly intervals
212 using an online device (TH-300B, Tianhong, China). Meteorological parameters,
213 including ambient temperature (T), relative humidity (RH), precipitation (PCP), wind
214 direction (WD), and wind speed (WS) were observed synchronously using an automatic

设置了格式: 字体: 加粗

设置了格式: 字体: 加粗

设置了格式: 字体: 非倾斜, 突出显示

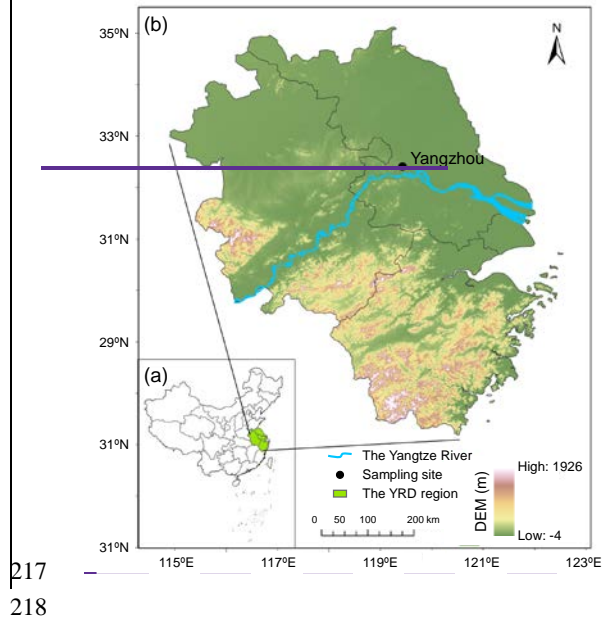
设置了格式: 突出显示

设置了格式: 字体: 非倾斜, 突出显示

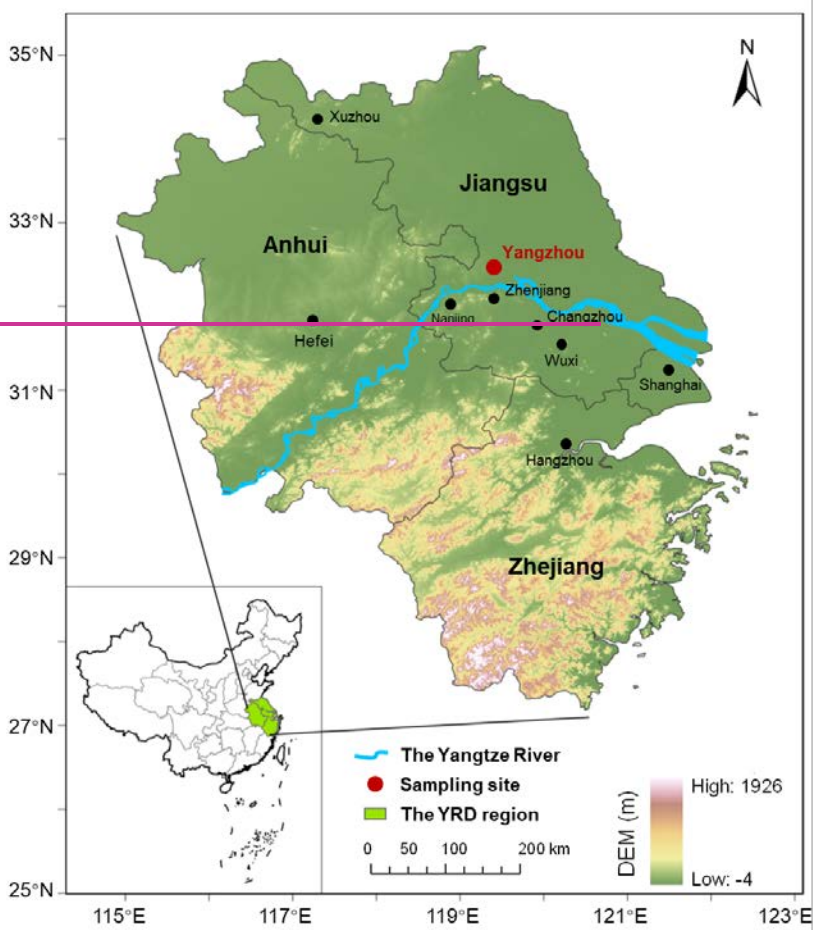
设置了格式: 突出显示

设置了格式: 字体: 非倾斜, 突出显示

215 weather instrument (WXT530, Vaisala, Finland). All online data presented in this paper
216 were hourly averaged at local time (Beijing time, UTC+8).



217
218



219
 220 **Figure 1.** Geographical overview of the Yangtze River Delta (YRD) Region in China.
 221 Location depicting the major cities within the YRD and the sampling site located in
 222 Yangzhou of the Yangtze River Delta (YRD) in China, (b) the sampling site in
 223 Yangzhou and the major cities of YRD. The color gradient from green to white indicates
 224 varying altitudes across the region. (Maps were generated by using ArcGIS Pro).

225 **3.4.2.2 -Data analysis**

226 **4.12.2.1 Satellite Product**

227 Remote sensing of nitrogen dioxide (NO₂) and sulfur dioxide (SO₂) using satellite has
 228 become a crucial tool for studying air pollution on a large spatial scale. In this study,
 229 we utilized the Copernicus Atmosphere Monitoring Service (CAMS) Global Near-
 230 Real-Time dataset (available at [https://developers.google.com/earth-](https://developers.google.com/earth-engine/datasets/catalog/ECMWF_CAMS_NRT)
 231 [engine/datasets/catalog/ECMWF_CAMS_NRT](https://developers.google.com/earth-engine/datasets/catalog/ECMWF_CAMS_NRT)), acquired from the European Centre
 232 for Medium-Range Weather Forecasts (ECMWF), to analyze the distribution of total

设置了格式: 突出显示

233 surface column concentrations of NO₂, SO₂ and surface PM_{2.5} mass concentration.
234 CAMS offers the capacity to continuously monitor the composition of the Earth's
235 atmosphere at global and regional scales since 2016. Level 3 Near Real Time Product
236 of NO₂ (NRTI/L3 NO₂) obtained from the TROPOspheric Monitoring Instrument
237 (TROPOMI) with a spatial resolution of 44528 meters (Benedetti et al., 2009; Morcrette
238 et al., 2009) 3.5×7 km² to analyze the distribution of total vertical column of NO₂
239 (Cooper et al., 2022). To avoid the obvious noises present in the NRTI/L3 SO₂ data over
240 clean regions, we employed the SO2SMASS band from the Modern Era Retrospective
241 Analysis for Research and Applications, version 2 (MERRA-2 SO2SMASS) with a
242 spatial resolution of 69×55 km² to represent the distribution of SO₂ surface mass
243 concentration (Ukhov et al., 2020). The details of the bands of the dataset used in this
244 study are shown in Table S2. We calculated and plotted the averaged 2-dimensional
245 data of ECMWF/CAMS/NRT NO₂, SO₂ and PM_{2.5} NRTI/L3 NO₂ and SO2SMASS
246 during BLD and LD over the region of interest (17.93~54.74 °N, 71.21~142.23 °E)
247 using Google Earth Engine (Gorelick et al., 2017). The integration of MERRA-2 and
248 TROPOMI remote sensing measurements has provided a more comprehensive
249 understanding of the sources and distributions of particle matter and of NO₂ and
250 SO₂ gaseous pollutants facilitating the evaluation of the impact of human activities on
251 air quality.

253 3.4.32.2.2 Geographic Source Analysis

254 The potential source contribution function (PSCF) analysis, based on the Hybrid
255 Single-Particle Lagrangian Integrated Trajectory (HYSPLIT) model, can be employed
256 to identify regional sources of air pollutants. Before conducting the PSCF analysis, 36
257 hours of air mass backward trajectories with one-hour resolution at 500 m above ground
258 level were calculated using the wind data from the Global Data Assimilation System
259 (GDAS) provided by the National Oceanic and Atmospheric Administration (NOAA)
260 (Wang et al., 2009). An open-source software MeteoInfo (Wang, 2014) was utilized for
261 the PSCF analysis. The whole study area (110.1~133.4 °E and 21.3~39.9 °N) covered
262 by the trajectories was divided into thousands of cells with a spatial resolution of 0.1°
263 × 0.1°. The PSCF was simulated according to the following equation:

$$264 \quad PSCF_{ij} = \frac{m_{ij}}{n_{ij}} \quad (1)$$

265 where $PSCF_{ij}$ is the conditional probability that the grid cell (i, j) was a source of the
266 species found in high concentration (Hopke et al., 1993); n_{ij} is the number of all
267 trajectories passing through this grid cell, and m_{ij} is the number of trajectories. In this
268 study, the pollution criterion values for different BCc particle types were set as the 75th
269 percentile of hourly average number fractions, respectively. To further improve the
270 accuracy of the PSCF analysis and minimize analytical uncertainties, the Weighted
271 PSCF (WPSCF) functions as shown in Equation (2~3) were applied (Polissar et al.,
272 1999). The weight (W_{ij}) for each grid cell was determined based on the number of

设置了格式: 突出显示

设置了格式: 突出显示

设置了格式: 突出显示

设置了格式: 突出显示

域代码已更改

273 trajectory endpoints (n_{ij}) as follows:

$$274 \quad WPSCF_{ij} = W_{ij} \times PSCF_{ij} \quad (2)$$

$$275 \quad W_{ij} = \begin{cases} 1.00 & n_{ij} > 3n_{ave} \\ 0.70 & 1.5n_{ave} < n_{ij} \leq 3n_{ave} \\ 0.40 & n_{ave} < n_{ij} \leq 1.5n_{ave} \\ 0.17 & n_{ij} \leq n_{ave} \end{cases} \quad (3)$$

276 Here, n_{ave} is the average number of trajectory endpoints of each grid.

277-4.4.2.3 SPA-MS Data Analysis

278 In total, 1649574 particles were analyzed during the entire observation period. The size
279 and chemical composition of single particles were analyzed using the Computational
280 Continuation Core (COCO V1.4) toolkit in MATLAB 2022 (The MathWorks, Inc.).
281 Our focus was on BCc, which ~~were was~~ identified based on the relative peak area (RPA)
282 of carbon ion clusters (C_n^+ , $n = 1, 2, 3, \dots$), with a threshold of 0.05 (Zhang et al., 2021).
283 An adaptive resonance theory-based neural network algorithm (ART-2a) was applied
284 to classify the measured individual particles based on the presence and intensity of ion
285 peaks, with a vigilance factor of 0.75, a learning rate of 0.05, and 20 iterations (Song et
286 al., 1999).
287

288 4.3. Results and discussion

289 4.13.1 Overview of field observations

290 **Figure 2** presents the temporal variations of meteorological parameters, $PM_{2.5}$, NO_x ,
291 and SO_2 concentrations ~~during the entire observation~~. ~~Notably, $PM_{2.5}$, NO_x , and SO_2~~
292 ~~were significantly reduced at the end of BLD due to a high precipitation event, and the~~
293 ~~data collected during the precipitation were excluded from the data analysis. During the~~
294 ~~BLD-stage~~, the mean temperature (T) was 28.2 ± 2.63 °C, with an average relative
295 humidity (RH) of $81.4 \pm 11.4\%$. The prevailing winds originated from the south and
296 southeast, with a mean wind speed (WS) of 3.4 ± 0.9 m s⁻¹. ~~Notably, $PM_{2.5}$, NO_x , and~~
297 ~~SO_2 were dramatically significantly reduced at the end of the BLD period due to a high~~
298 ~~precipitation event, and the data collected during the precipitation were excluded from~~
299 ~~the analysis~~. In comparison, LD ~~saw shows~~ a decline in temperature to 26.2 ± 2.4 °C, ~~a~~
300 ~~reduction in and~~ WS to 2.3 ± 0.8 m s⁻¹, ~~and but~~ an increase in RH to $86.67 \pm 10.4\%$.
301 ~~Additionally, Figures S2b- and c exhibit present~~ uniform distributions of RH and
302 boundary-layer height (BLH) across the YRD during LD. ~~The implication is that The~~
303 ~~the~~ resemblance of regional meteorological ~~elements conditions with other cities in the~~
304 YRD (Qian et al., 2022; Wang et al., 2022) and, the effective removal of the pollutants
305 accumulated ~~during at the end of BLD-stage~~, provides a favorable condition for
306 ~~investigating the regional transport of BCc during imply LD in that Yangzhou is mainly~~
307 ~~affected by upwind transmission during LD, providing favorable conditions for~~
308 ~~investigating the regional transport of BCc in the YRD during summer. During ALD,~~

设置了格式: 字体: 加粗

设置了格式: 字体: 倾斜

设置了格式: 字体: 加粗

设置了格式: 字体: 加粗

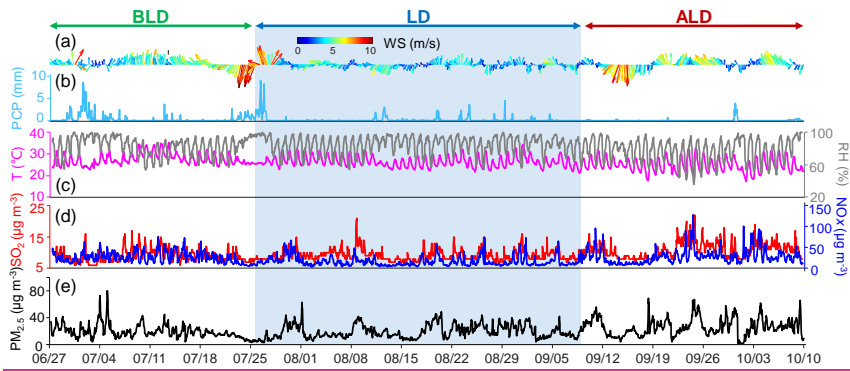
309 ~~Subsequently,~~ the temperature declined to 25.2 ± 3.5 °C, the WS increased to 3.2 ± 1.4 m
 310 s^{-1} , and RH decreased to a lower level of $74.75 \pm 15.0\%$ ~~during the ALD period.~~

314 Surface concentrations of NO_x ($18.99 \mu g m^{-3}$) and TVOC ($55.096 \mu g m^{-3}$) were the
 315 lowest during LD compared to those of ~~the~~ BLD and ALD ~~periods~~, whereas the surface
 316 O_3 concentration showed an increase of $12.63 \mu g m^{-3}$ (19%) during LD compared ~~to the~~
 317 ~~BLD₂ period T,~~ ~~which may attribute to potentially due to~~ the reduction of fresh NO
 318 ~~emissions that alleviates~~ O_3 titration (Steinfeld, 1998) ~~could be an explanation.~~
 319 ~~Furthermore, a~~ Analysis from ~~Figure S5-S3~~ indicates that the O_3 ~~ozone level in~~
 320 ~~Yangzhou was slightly higher than that~~ of neighboring cities ~~other major cities in~~
 321 ~~the YRD, highlighting~~ suggesting higher atmospheric oxidizing capacity ~~in the~~
 322 ~~Yangzhou atmosphere~~ during LD. However, the average concentrations of $PM_{2.5}$ (19.9
 323 vs. $21.2 \mu g m^{-3}$) ~~and~~ SO_2 (9.4 vs. $9.5 \mu g m^{-3}$), ~~and~~ CO (0.61 ~~and~~ vs. $0.64 mg m^{-3}$), ~~and~~
 324 ~~TVOC~~ (58 vs. $56 \mu g m^{-3}$) were ~~comparable~~ very close between during both BLD and
 325 LD stages (Figure 3).

327 ~~Following the end of~~ After the lockdown LD, social activities gradually resumed ~~in~~
 328 Yangzhou City, leading to an apparent increase in all observed pollutants during the
 329 ALD period. For instance, there ~~were~~ relative increases ~~from LD to ALD of were~~ 71%
 330 for NO_x , 22% for SO_2 , 55% for TVOC, 30% for O_3 , 29% for $PM_{2.5}$, and 17% for CO
 331 ~~from LD to ALD~~ 29% for $PM_{2.5}$ (Figure 3), respectively (Figure 3). Given that both BC
 332 and CO are byproducts of incomplete combustion of carbon-based ~~containing~~ fuels
 333 (Wang et al., 2015), and ~~considering~~ the high correlation between BC and CO (Zhou et
 334 al., 2009), it is plausible to infer that the primary emission source of BC during LD was
 335 ~~different with from~~ that during ALD.

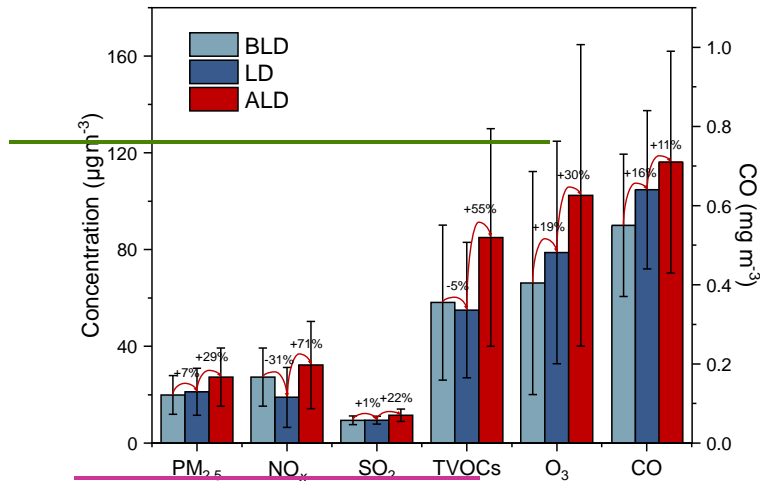
- 设置了格式: 字体: 加粗
- 设置了格式: 字体: 加粗
- 设置了格式: 突出显示
- 设置了格式: 上标, 突出显示
- 设置了格式: 突出显示
- 设置了格式: 字体: 加粗, 突出显示
- 设置了格式: 突出显示
- 设置了格式: 非上标/ 下标
- 设置了格式: 突出显示
- 设置了格式: 突出显示
- 设置了格式: 突出显示
- 设置了格式: 突出显示

336

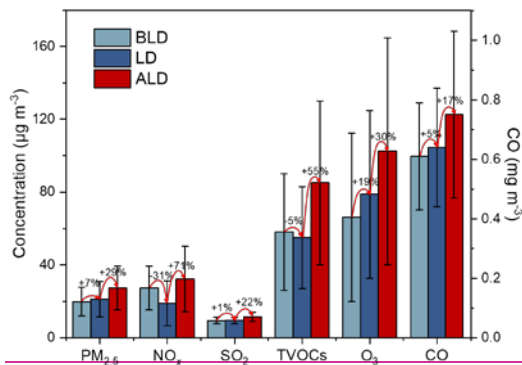


337
 338 **Figure 2.** Temporal variations of (a) wind direction (WD) and wind speed (WS), (b)
 339 precipitation (PCP), (c) temperature (T) and relative humidity (RH), (d) concentrations
 340 of NO_x and SO_2 , and (e) mass loading of $PM_{2.5}$. The green, blue, and red arrow ranges

341 denote the periods before lockdown (BLD), during lockdown (LD), and after lockdown
 342 (ALD).



343



344 **Figure 3.** Ground-based observations of PM_{2.5}, NO_x, SO₂, O₃, CO, and TVOC
 345 concentrations in Yangzhou. The figure compares the averages during the BLD (blue-
 346 grey), LD (dark blue), and ALD (crimson) periods. Error bars indicate SDs over
 347 different lockdown periods.
 348

349 In addition to ground measurements, satellite-retrieved PM_{2.5}, NO₂, and SO₂
 350 data over the entire region of eastern China were also investigated, and Results results
 351 show that the hotspots of these pollutants were predominantly located
 352 concentrated over in eastern China, e.g., the YRD Shanghai and its neighboring cities,
 353 including Yangzhou region, during both the BLD and LD periods (Figure 3S4). Figure
 354 4 displays presents the regional fractional changes, including Yangzhou, in of mean
 355 PM_{2.5}, NO₂, and SO₂ levels-concentrations from the BLD to LD periods in the YRD,
 356 all showing indicating an increase of 29.0%, 6.0%, and 13.84% increase, respectively.
 357 In comparison, Yangzhou city experienced lower increases in these air pollutants, with
 358 slight changes of 6.0%, -18.0%, and -4.3% for PM_{2.5}, NO₂, and SO₂, respectively

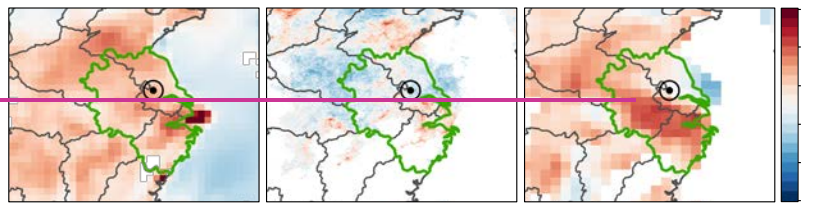
设置了格式: 字体: 加粗
 设置了格式: 字体: 加粗

359 (~~remarkable NO₂ decrease~~). The implication is that, even though local primary
 360 emissions, such as NO₂ and SO₂, were reduced ~~dramatically~~ substantially during LD,
 361 they still could be affected by regional transport. ~~While some discrepancies existed~~
 362 ~~between~~ Although, there existed some error between the spaceborne and ground
 363 measurements, ~~but these results still provide valuable insights into the pollution trends~~
 364 ~~during the entire lockdown period~~ those results also can show the pollution tendency
 365 during the whole lockdown period. Furthermore, as depicted in ~~In additional, as~~
 366 ~~illustrated in Figure S5S43~~, ~~The the~~ levels concentrations of PM_{2.5}, NO₂, and CO of
 367 ~~in the those~~ major cities of the YRD ~~was were~~ more than twice higher than those in
 368 Yangzhou during LD, ~~especially particularly~~ the NO₂, ~~indicating confirming~~ a relatively
 369 lower level of local primary emissions in Yangzhou compared to other major cities due
 370 to the stringent lockdown ~~measures~~, which means the primary emission was attenuated
 371 in Yangzhou compared with other major cities because of the stringent lockdown
 372 measures. ~~Additionally~~ However, the higher level of SO₂ in Yangzhou during LD may
 373 be attributed to the nearby power stations along the Yangtze River, which were not
 374 impacted by the lockdown measures. ~~These findings underscore~~ Such results highlight
 375 the short term, limited scale, and human induced reduction in air pollutants as a ~~r~~
 376 ~~resulting from of the lockdown measures in Yangzhou and demonstrate~~ highlighting
 377 the effectiveness of regional stringent emission control in reducing local atmospheric
 378 ~~gaseous pollutant concentrations~~.

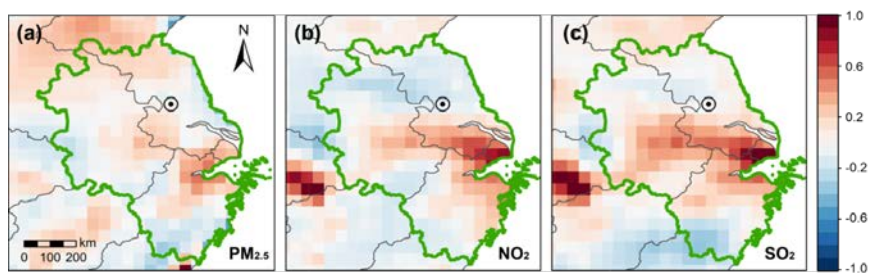
设置了格式: 下标

设置了格式: 下标

379



380



381

382

383 **Figure 4.** The fractional changes (i.e., $100 \times (\text{LD} - \text{BLD}) / \text{BLD}$) of (a) PM_{2.5}, (b) NO₂,
 384 and (c) SO₂ between BLD and LD periods based on spaceborne measurement. The
 385 circle symbols in the maps indicate the location of Yangzhou, and the green region
 386 represents the YRD.

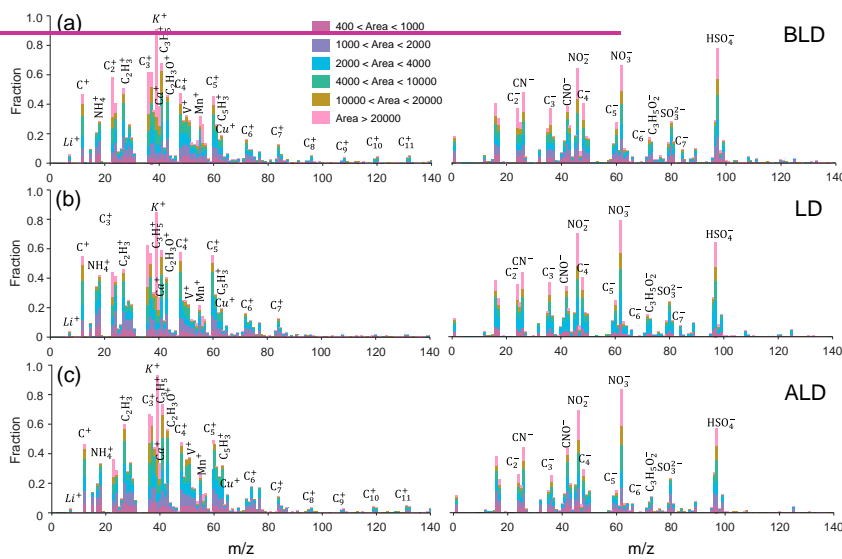
387 4.63.2-Chemical composition and size distribution of
388 individual BCc

389 Based on the SPA-MS analysis, a total of 1068362 BCc ~~were~~was collected ~~over~~during
390 the whole study period. The BCc accounted for 58.89%, 67.79%, and 56.57% of the
391 total number of measured particles in the BLD, LD, and ALD periods, respectively.

392 **Figure 5** shows the normalized average mass spectra of BCc during three periods. Ion
393 height in each spectrum reflects the number fraction of the detected BCc with the
394 corresponding ion to the total BCc, while colors represent peak area ranges of detected
395 ions. **As shown in Figure 5**, BCc in BLD, LD, and ALD shown similar mass spectra at
396 $m/z < 100$, with common peaks including carbon ion clusters (C_n^{\pm} , $n = 1\sim 7$), m/z
397 $27[C_2H_3]^+$, $37[C_3H]^+$, $43[C_2H_3O]^+$, $51[C_4H_3]^+$, $63[C_5H_3]^+$, $46[NO_2]^-$, $62[NO_3]^-$, and
398 $97[HSO_4]^-$. However, the abundance of large m/z carbon ions (C_n^{\pm} , $n > 7$) in both BLD
399 and ALD periods was ~~approximately~~1.5 times **higher than** that in the LD. **Previous**
400 **studies have indicated that high-mass carbon ions may be linked to traffic emissions,**
401 **particularly those from diesel trucks(Xie et al., 2020; Liu et al., 2019), and t****he**
402 **observed reduction in such ions during LD suggests a decrease in local vehicle**
403 **emissions. This trend is also consistent with the changes observed in aromatic**
404 **compounds, e.g. m/z 119 $[C_9H_{11}]^+$.**

405

406

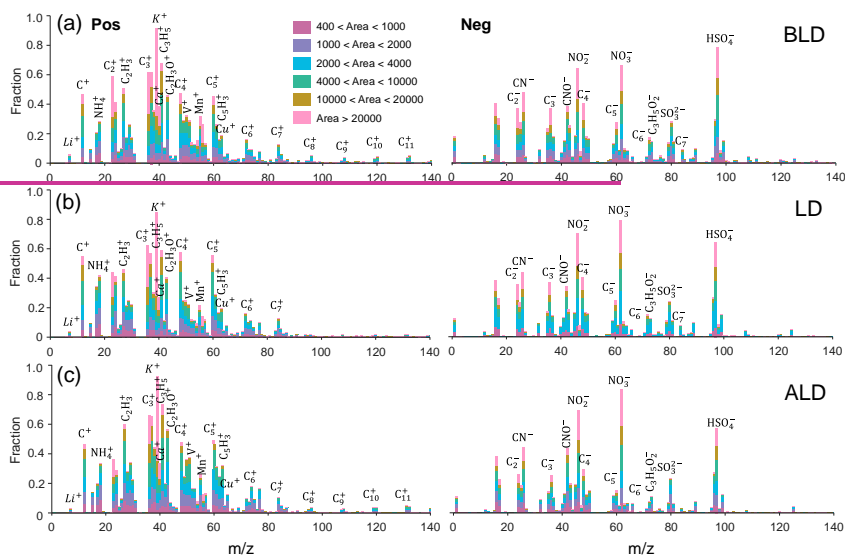


设置了格式: 字体: 加粗

设置了格式: 突出显示

设置了格式: 突出显示

带格式的: 正文, 段落间距段后: 0 磅



407
408 **Figure 5.** The average positive and negative mass spectra of BCCs (a) before the
409 lockdown period (BLD), (b) during the lockdown period (LD), and (c) after the
410 lockdown period (ALD).

411
412 Further, BCCs were further classified into 12 types based on the differences in
413 chemical features and temporal variations, as shown in Table S1. Fresh BC particles
414 (BC-fresh) are those freshly emitted without undergoing significant atmospheric
415 processing (Ding et al., 2021). Five types of BC-fresh particles were identified
416 according to their characteristics-ion markers: (i) BC-pure is dominated by carbon
417 clusters (C_n^+) with minor ion signals of secondary-inorganic species, such as m/z
418 46[NO₂]⁻ and m/z 97[H₂SO₄]⁻ from nitrate and sulfate, respectively (Xie et al., 2020);
419 (ii) BCCs from biomass burning (BB) are characterized by ion signals at m/z 39[K]⁺,
420 45[CHO₂]⁻, 59.59[C₂H₃O₂C₂H₃O₂]⁻, and 73[C₃H₅O₂]⁻, with a relative peak area (RPA)
421 more than 0.5 (Silva et al., 1999); (iii) coal combustion BCCs (CC) typically include
422 small carbon clusters (C_n^+ , n = 1~4), metal elements (e.g., m/z 7[Li]⁺, 23[Na]⁺, 27[Al]⁺,
423 56[Fe]⁺, 63[Cu]⁺ and 206/207/208[Pb]⁺), and organic carbon (38[C₃H₂]⁺, 43[C₂H₃O]⁺)
424 peaks in the positive mass spectrum, while the strong signals of secondary inorganic
425 species (46[NO₂]⁻, 43[AlO]⁻, 62[NO₃]⁻, 80[SO₃]⁻, 97[H₂SO₄]⁻) in the negative ion
426 mode suggest that CC particles were long-distance transported or more processed
427 (Zhang et al., 2022; Zhang et al., 2009); (iv) particles from vehicle emission (VE)
428 are characterized by the presence of ion signals at m/z 40[Ca]⁺, 51[V]⁺, 55[Mn]⁺,
429 67[VO]⁺, 46[NO₂]⁻, 62[NO₃]⁻, and 79[PO₃]⁻, as well as high loadings of organic carbon
430 (41[C₃H₅]⁺, 43[C₂H₃O]⁺) and carbon clusters (C_n^+ , n = 1~4) ion peaks (Yang et al., 2017);
431 (v) BCCs that are internally mixed with more than one type (BB, CC, and VE) are

设置了格式: 字体: 加粗

设置了格式: 非上标/ 下标

设置了格式: 非上标/ 下标

432 categorized as Mix type (Sun et al., 2022).

433
434
435 Aged BC particles, denote as BC-aged, undergo a series of chemical reactions and
436 physical transformations. These processes typically lead to changes in their morphology,
437 hygroscopicity, and optical properties as they are coated with other materials (He et al.,
438 2015). Six types of BCc are classified as BC-aged and are further grouped into BCOC
439 and BC-SNA, depending on whether they contain mainly organic carbon (OC) or
440 sulfate/nitrate/ammonium (SNA). First, BCOC types indicate BC-aged particles that
441 are internally mixed with OC. These particles are characterized by the presence of
442 carbon clusters (C_n^+) and $C_nH_m^+$ ions ($n = 1\sim6$, $m = 1\sim3$) in positive mass spectra (Xie
443 et al., 2020). On the other hand, BC-aged particles that do not mix with OC are named
444 BC-SNA indicating the mix with secondary inorganic species. Additionally, BCOC
445 particles with negative mass spectra dominated by nitrate ions ($46[NO_3^-]$ and
446 $62[NO_3^-]$) or sulfate ions ($97[HSO_4^-]$) are referred to as BCOC-N or BCOC-S,
447 respectively; otherwise, BCOC particles showing similar peak areas of nitrate and
448 sulfate are named BCOC-SN. Furthermore, The BC-SNA particles are further
449 categorized as BC-N, BC-S, and BC-SN based on similar principles. Note the
450 remaining particles that cannot be classified into either BC-fresh or BC-aged ones are
451 denoted as BC-other. More details of BCc particle types are shown in **Table S1** and
452 **Figure S1** in the Supplement.

453
454
455 During the BLD period, the average number fraction of BC-fresh particles was 36%
456 with sizes mainly concentrated at ~500 nm, while, similar to the mode size of BC-aged
457 particles was ~520 nm (Figure 7). The predominant BCc types during the BLD
458 period were BCOC-S and BC-S (24% and 12% by number), likely because sulfate
459 was removed less efficiently than organic matter (OM) and NO_3 by heavy precipitation,
460 especially during the warm seasons (Isokääntä et al., 2022). As shown in Figures 7e
461 Figures 6c and d, the peak size of BC-SNA was larger than that of BCOC in all periods,
462 indicating that organics coated BCc generally had a relatively thin coating compared to
463 those coated by secondary inorganic species, which is consistent with previous studies
464 (Sun et al., 2016; Wang et al., 2019).

465
466 During the transition of BLD period ($PM_{2.5}$: $19.9 \mu g m^{-3}$, O_3 : $66.2 \mu g m^{-3}$, NO_x : $27.3 \mu g$
467 m^{-3}) to LD period ($PM_{2.5}$: $21.2 \mu g m^{-3}$, O_3 : $78.8 \mu g m^{-3}$, NO_x : $18.9 \mu g m^{-3}$), heavy
468 precipitation occurred on from the evening of July 27th and early morning of July
469 28th (the day before eve of lockdown), resulting in the removal of a majority of the
470 pollutants and scavenged a majority of the pollutants ($PM_{2.5}$: $4 \mu g m^{-3}$, O_3 : $35 \mu g m^{-3}$,
471 NO_x : $8 \mu g m^{-3}$). After that, strict lockdown measures were carried on and the primary
472 emissions were abruptly cut down. As a result, the number fraction of BC-fresh
473 particles significantly decreased from 37% to 28% and that of VE-type particles

设置了格式: 字体: 加粗

设置了格式: 字体: 加粗

带格式的: 缩进: 首行缩进: 0 厘米

设置了格式: 字体: 加粗

设置了格式: 字体: 加粗

设置了格式: 字体: 加粗

设置了格式: 突出显示

设置了格式: 上标, 突出显示

设置了格式: 突出显示

474 dropped from 12% to 3% (by number). As shown in Expectedly Figure 3, with the
475 decrease in NO_x, an obvious enhancement of O₃ was observed during LD (Figure 3).
476 According to previous studies (Huang et al., 2021; Laughner et al., 2021), large
477 reduction of NO_x could may promote the formation of O₃ under a VOC-limited regime
478 and enhance the oxidation capacity of the local atmosphere, which may made-promote
479 the number fraction of BC-aged particles increased from 64% in the BLD to 72% in
480 LD (Figure 6a Figure 7a), indicating the lockdown measures could accelerate aging of
481 BCc through complicated chemical reactions and/or physical coagulation. We also
482 found + Additionally, the most abundant type of BCc changed from BCOC-S (24% by
483 number) in the BLD to BC-N (25%) in the LD (Figure 6a Figure 7a), suggesting
484 different BCc formation pathways. Furthermore, d Despite the abrupt reductions of NO_x
485 due to the city lockdown, it should be aware that the PM_{2.5} concentration slightly
486 increased during LD, highlighting the non-linear relationship between primary
487 emissions and PM_{2.5} levels.

488
489 During the ALD period (PM_{2.5}: 25.96 μg m⁻³, NO_x: 27.98 μg m⁻³, TVOC: 76.4 μg m⁻³),
490 the number fraction of BC-fresh particles increased-rose from 28% (LD) to 31% (ALD),
491 and while the fraction of VE particles also increased from 3% (LD) to 12% (ALD) (by
492 number) (Figure 6a Figure 7a). Notably, the size distributions of BC-fresh and BC-
493 aged particles presented relatively small peaks at 690 nm and 820 nm during the ALD
494 period, in addition to the prominent peaks at 490 nm and 500 nm, which were different
495 from those in the BLD and LD periods. These small peaks were relatively close to the
496 dominant sizes of BC-fresh and BC-aged particles during LD (Figure 7 Figure 6). This
497 result suggests that a substantial number of BCc with small sizes (around 500 nm) after
498 the lockdown was lifted in Yangzhou, owing to the sudden enhancement of primary
499 emissions; on the other hand, particles with large diameters (>690 nm) may have
500 formed due to the participation of more trace reactive gases (e.g., NO_x, SO₂, and VOCs)
501 in continuous aging reactions, resulting in thicker coatings on the surface of pre-existing
502 particles and therefore a more clear separation of two-mode sizes during the ALD
503 period than during the other two periods. This hypothesis was also supported by the
504 increased number fraction of BCOC-SN during the ALD period (Figure 6a Figure 7a).
505 Similar findings have been reported in the North China Plain (NCP) and the YRD
506 during cold seasons, where thicker coatings on secondary aerosols were also observed
507 under lower RH (<70%) (Zhang et al., 2021). This might be due to that particles with
508 more organics and nitrate can result in earlier deliquescence and provide aqueous
509 surfaces that facilitate the heterogeneous formation of secondary species under
510 relatively low RH (Zhang et al., 2021). Among the three periods, the difference between
511 the mode sizes of BC-aged and BC-fresh particles was the smallest (10 nm) during the
512 ALD period (Figure 7a Figure 6a and b). This size reduction can be attributed to the
513 increased BCOC and hydrophobic primary particles after lockdown (Figure 6 Figure 7).
514 Because the internally mixed BCOC and hydrophobic primary particles may constrain
515 further growth of secondary BC-SNA particles (Liu et al., 2016; Zhang et al., 2018),

设置了格式: 字体: 加粗

设置了格式: 字体: 加粗

设置了格式: 字体: 加粗

设置了格式: 字体: 加粗

设置了格式: 字体: 加粗

设置了格式: 非突出显示

设置了格式: 非突出显示

设置了格式: 非突出显示

设置了格式: 非突出显示

设置了格式: 字体: 加粗

设置了格式: 字体: 加粗

设置了格式: 字体颜色: 自动设置

设置了格式: 字体颜色: 自动设置

设置了格式: 字体颜色: 自动设置

域代码已更改

516 thereby leading to smaller-sized BC-aged particles. Moreover, the differences in BCc
517 mode sizes between ALD and BLD periods also reveal an interesting fact that the
518 lockdown effect may not only affect air quality during lockdown but also can influence
519 the air quality even after lockdown, as the resumed emissions after lockdown may be
520 subjected to different chemistry from that before lockdown.

521
522
523

524 Throughout the entire observation, the changes in the number fraction of BC-SNA
525 ~~showed~~ exhibited consistency with the variations in RH (~~Figure 6b~~ Figure 7b),
526 indicating that BC tends to mix with ammonium sulfate and ammonium nitrate under
527 high RH conditions ~~overall~~. Meanwhile, the number fraction of BCOC ~~had~~ shows
528 similar patterns ~~of change~~ as TVOC, suggesting that high TVOC levels may facilitate
529 the coating of organics on BC cores under low RH condition.

530 Figure 8 displays the number fraction of BCc species as a function of PM_{2.5}. Overall,
531 as PM_{2.5} levels increased, the number fraction of BC-aged particles also increased,
532 while the proportion of BC-fresh particles decreased during ~~the~~ BLD and LD ~~periods~~,
533 indicating a clear transition from BC-fresh particles to more aged ones, in line with the
534 average size distribution during ALD has a small peak at 900 nm. Specifically, However,

535 ~~the~~ increase in PM_{2.5} was driven by BCOC-S during ~~the~~ BLD ~~period~~ (Figure 8a),
536 whereas BC-N played a vital role in the PM_{2.5} increase during LD (Figure 8b).
537 Interestingly, the concentration of NO_x, the primary precursor of BC-N, decreased by
538 31% and 41% during LD compared to ~~the~~ BLD and ALD ~~periods~~, respectively (Figure

539 3). ~~Despite the significant decrease, the proportion of BC-N during LD was~~
540 unexpectedly higher than those during the BLD and ALD periods, indicating a strong
541 non-linear response of nitrate in BCc to NO_x, ~~very~~ likely due to much faster conversion
542 of NO_x to nitrate upon enhanced atmospheric oxidation capacity; additionally, the high
543 proportion of BC-N during LD might be attributed to regional transport, similar to that
544 in Shanghai during 2020 winter lockdown (Chang et al., 2020).

设置了格式: 字体: 加粗

设置了格式: 字体: 加粗

设置了格式: 字体: 加粗

设置了格式: 图案: 清除

设置了格式: 字体: 加粗

设置了格式: 字体: 加粗

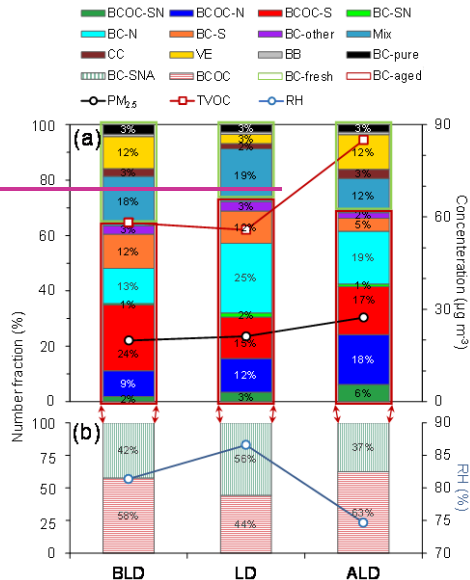
设置了格式: 字体: 加粗

设置了格式: 字体: 加粗

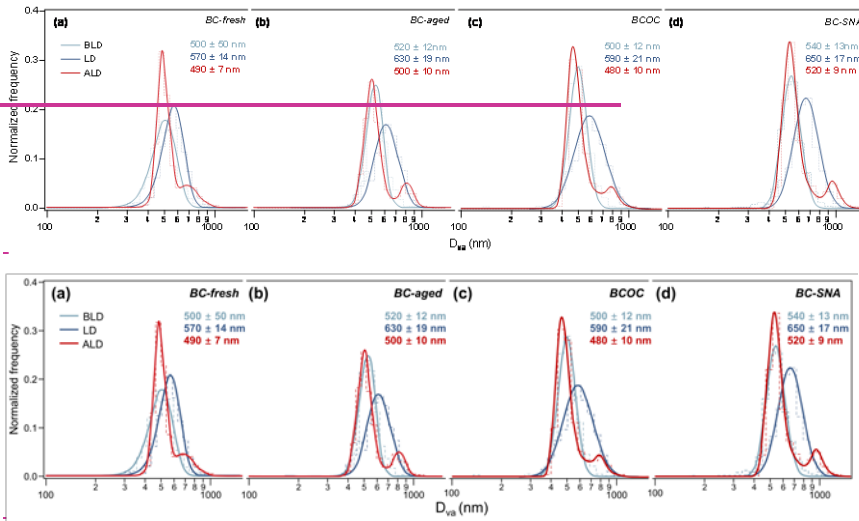
设置了格式: 字体: 加粗

设置了格式: 字体: 加粗

设置了格式: 字体: 倾斜



545
 546 **Figure 6.** Number fractions of BCe. (a) The number fractions of different BCe along
 547 with the concentrations of PM_{2.5} and total volatile organic compounds (TVOC). (b)
 548 The number fractions of different types of BC aged particles along with relative
 549 humidity (RH).



550
 551
 552 **Figure 7.** Size distribution of different types of BCe during different periods in
 553 Yangzhou. (a) BC fresh particles, (b) BC aged particles, (c) BCO, and (d)
 554 BC SNA particles. The Log-normal distribution was used to fit the unimodal size
 555 distribution, and the Lorentz distribution was used to fit the bimodal size
 556 distribution. The corresponding mode sizes (with the standard deviations) are also shown.

带格式的: 正文, 段落间距段后: 0 磅

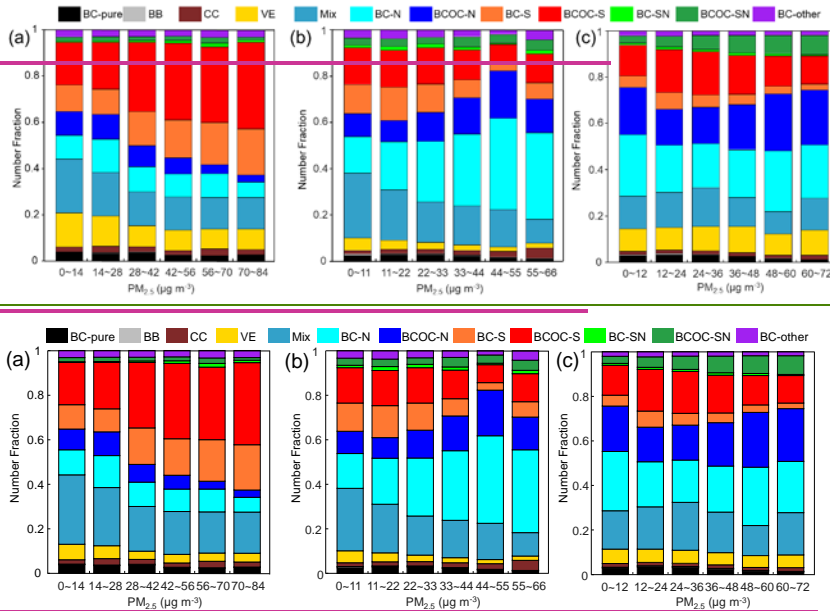


Figure 8. Variations of number fractions of BCe particle types with $PM_{2.5}$ -mass concentrations during (a) the BLD period, (b) LD, and (c) the ALD period.

4.93.3 -Chemical aging of BCc

As shown in **Figure 5**, in the average positive mass spectra of total BCc, the peak areas of C_n^+ , OM, and metals contributed to more than 95% of the total, while nitrate and sulfate peak areas accounted for more than 90% of the negative mass spectral signal. To better elucidate the aging processes of BCc during different lockdown periods, we summed the carbon clusters C_n^+ ($n = 1\sim 5$, accounting for more than 99% of C_n^+) peak areas to represent BC, and the total peak area of sulfate, nitrate, and ammonium (SNA) to represent the second inorganic components coated on BC. Additionally, we defined the sum of positive peak areas, excluding C_n^+ and metals, as OC to represent the OM coated on BC. These peak areas encompassed almost all the coating materials, except for metals, of BCc. The changes in the mixing state and morphology of BCc can provide insights into their aging characteristics, as reported previously (Kandler et al., 2018; Moffet et al., 2013). In this study, we use OC/C_n and SNA/C_n ratios to describe different types of chemical components coated on BC-fresh, and we use the ratio of the mode size of BC-aged (D_{aged}) to that of contemporaneous BC-fresh (D_{fresh}) to represent the aging degree of BCc.

Figure 9 illustrates the diurnal variations of the OC/C_n and SNA/C_n ratios along with the size distribution of BCc during different periods. **Throughout the entire observation,**

设置了格式: 字体: 加粗

设置了格式: 字体: 加粗

582 ~~w~~We observed that both OC/C_n and SNA/C_n increased during nighttime and decreased
583 during daytime. These variations showed the prominent enhancements of nocturnal OM
584 and SNA, which could be attributed to the accelerated gas-to-particle partitioning and
585 nocturnal secondary formation of organic/inorganic components under high relative
586 humidity (RH > 85%) and relatively stagnant air ~~mass~~ (WS < 3 m s⁻¹) (**Figure S4S5**).
587 It is worth noting that from ~~the-BLD-period~~ to ~~the-LD~~ and ~~ALD-periods~~, the intensity
588 of diurnal variations of OC/C_n and SNA/C_n increased obviously. This discrepancy can
589 be attributed to several reasons. (i) ~~During the-BLD-period~~, the frequent precipitations
590 effectively scavenged the particles (Isokääntä et al., 2022); (ii) ~~In contrast~~, stronger
591 solar radiation and higher ~~ozone-O₃ levels-concentration~~ during LD promoted
592 photochemical formations of OC and SNA; (iii) After lockdown, more precursors due
593 to increased local emissions may lead to more production of secondary components
594 than that during ~~the BLD-period~~ as explained earlier. These results indicate that the
595 aging process and mixing state of BCc depend strongly on ~~meteorological~~
596 ~~conditionsweather conditions andas well as anthropogenic-emission structures-sources~~
597 in urban cities.

设置了格式: 字体: 加粗

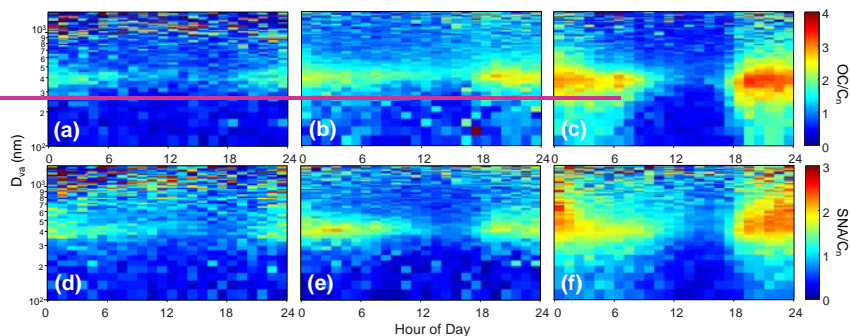
设置了格式: 下标

599 As shown in **Figure 9**, BCc with ~400 nm D_{va} exhibited significant diurnal fluctuations
600 in the OC/C_n and SNA/C_n ratios, during LD. ~~Moreover, t~~There ~~was-is~~ a noticeable
601 increase in the proportion of BC-SNA particles during nighttime when RH ~~was-is~~
602 relatively high. These observations suggest that nighttime heterogeneous hydrolysis
603 may be considered a key mechanism responsible for the formation of BCOC and BC-
604 SNA particles. According to Jacobson (2002), coagulation can be significant between
605 particles with sizes <100-nm and >1-μm but insignificant for particles of >300-nm,
606 when the total particle number concentration is higher than 10⁴ -cm⁻³. During LD, the
607 OC/C_n and SNA/C_n ratios of BCc with ~400 nm D_{va} exhibited pronounced diurnal
608 variations (**Figure 9**) and the number fraction of BC-SNA increased obviously. Despite
609 the difference between D_{va} and physical diameter, such results imply that chemical
610 reactions should be considered as the major pathway for BCOC and BC-SNA particles
611 of ~400 nm D_{va}, while the large-sized BC-aged particles (>1-μm) may be partially
612 from physical coagulation. ~~Moreover~~Additionally, the larger ~~mode~~ peak ~~D_{va}~~ (~600 nm,
613 D_{va}) and higher D_{aged}/D_{fresh} ratios (1.11) were observed compared to those of ~~the-BLD~~
614 (~510 nm, 1.03) and ~~the-ALD periods~~ (~500 nm, 1.02) (~~Figure-7~~**Figure 6**). Since RH
615 was significantly higher during LD (average RH of 86.67%) than ~~the-BLD-period~~**BLD**
616 (average RH of 81.4%) and ALD period (average RH of 74.75%), this result again
617 supports that aqueous or heterogeneous reactions might play a more important role to
618 facilitate the chemical conversion of trace reactive gases (e.g., SO₂, NO_x, and VOCs)
619 and then formed a thicker coating on the surfaces of BC cores, leading to evident growth
620 in the size of BCc. ~~In-addition, t~~This aqueous or heterogeneous process during LD likely
621 converted partially coated particles to fully thickly coated BCc as well (~~Figure-11~~).
622
623

设置了格式: 字体: 加粗

域代码已更改

设置了格式: 字体: 加粗



624
625 **Figure 9.** Diurnal variations of the ratios of OC/C_n and SNA/C_n with a size distribution
626 of BCc during (a, d) the BLD period, (b, e) LD, and (c, f) the ALD period.

627 4.123.4 -Source apportionment of BCc during lockdown

628 In addition to local emissions, regional transport plays a significant role in influencing
629 pollutant levels. ~~Due to~~ The emergent lockdown in Yangzhou, led to strict limitation
630 on local emissions were strictly limited, while surrounding cities were still running as
631 usual, ~~it is therefore interesting to investigate source areas of BCc sources under such a~~
632 scenario. This is supported by **Figure S6**, which illustrates the PM_{2.5} concentrations in
633 Yangzhou and the other five surrounding YRD cities (e.g., Nanjing, Zhenjiang,
634 Changzhou, Taizhou, and Chuzhou) during the campaign. High correlations between
635 PM_{2.5} concentrations in Yangzhou and the other five cities were observed across all
636 different periods (**Figure S6**). These findings underscore the importance of the regional
637 transport in PM_{2.5} pollution during the campaign. ~~Besides, the air pollutants were~~
638 significantly influenced by regional transport (**Figure 10**), presenting providing an ideal
639 unique opportunity to investigate the transmission and source characteristics of BCc in
640 the YRD during summer. Herein, ~~the PSCF method analysis was used applied~~ to
641 qualitatively simulate the source probability distributions of the specific BCc particle
642 types (BC-fresh, BC-aged, BCOC, and BC-SNA) during LD. ~~The results of the~~
643 potential source regions and clustering analysis are presented in Figure 10.

644
645 As shown in **Figure 10**, the hotspots of potential sources for the four particle types
646 exhibited strong agreements with each other and primarily concentrated in the southeast
647 of Yangzhou, especially along the coast of the Yangtze River, with the WPSCF greater
648 than 0.6. These hotspot areas also encompassed chemical enterprises, power plants,
649 petrochemical industrial parks, and the Yangtze River ~~Ship Channel~~ in the YRD.
650 ~~Moreover, BCc and gaseous emissions from the YRD city cluster, heavy industries, and~~
651 ~~ship diesel engines can easily impact the air quality of surrounding downwind regions.~~
652 This evidence suggests that the region of southeast Yangzhou and lower reaches of the
653 Yangtze River are major source areas for the regionally transported BCc in Yangzhou
654 during lockdown.

设置了格式: 下标

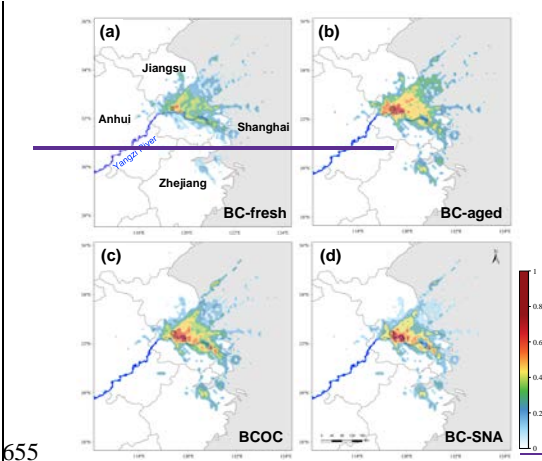
设置了格式: 下标

设置了格式: 下标

批注 [WJ1]: 引图 10 作证据, 或者刚刚画的区域城市那个时间序列图

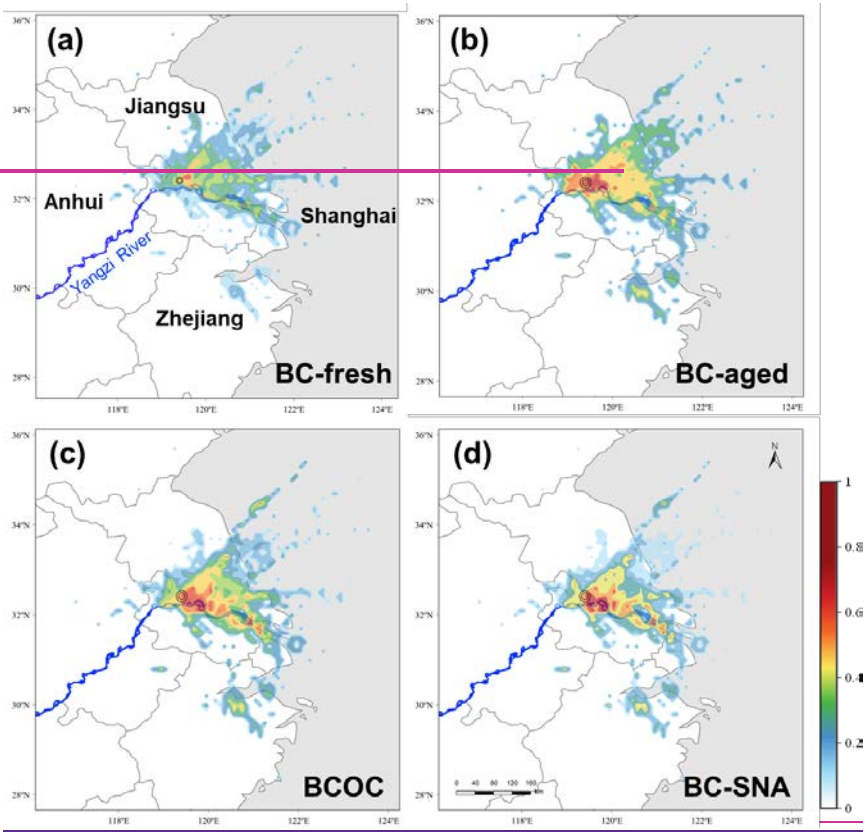
设置了格式: 字体: 加粗

批注 [WJ2]: 没数据, 删了



655
656

Additionally,



657
658
659

Figure 10. The potential sources areas of different BCe during LD. (a) BC-fresh. (b) BC-aged. (c) BCOC. (d) BC-SNA.

带格式的: 两端对齐, 缩进: 左 0 字符

660 According to Luo et al. (2023), reported that regional transport of pollutants can occur
 661 near the surface from upwind areas when the wind speed (WS) exceeds 2 m s^{-1} . Figure
 662 S4b-S5b shows that the mean daytime WS was 3 m s^{-1} , indicating that both BC-fresh
 663 and BC-aged particles, along with trace gases (e.g., SO_2 , NO_x , and VOCs), originating
 664 from the hotspot areas, could be transported effectively to Yangzhou. Additionally, the
 665 average size of BCc remained around $0.6 \mu\text{m}$ at daytime (Figure S4eS5c),
 666 suggesting that BCc could undergo continual aging reactions under relatively lower RH,
 667 but produce relatively thinly coated BCc with smaller sizes than those at nighttime
 668 (average size of $0.65 \mu\text{m}$) (Figure 11). The mean nocturnal WS decreased to 2 m s^{-1} ,
 669 indicating that the regional atmosphere becomes stagnant (Figures S4aS5a, b). As
 670 mentioned earlier and underscored here again, this stagnant and humid atmospheric
 671 condition may promote aqueous or heterogeneous reactions, likely further leading to
 672 the production of more thickly coated BCc than daytime ones (Figure 11).

设置了格式: 字体: 加粗

设置了格式: 字体: 加粗

设置了格式: 字体: 加粗

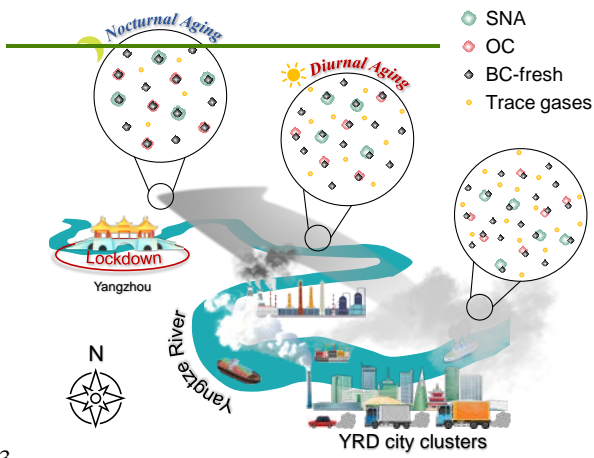
设置了格式: 字体: 加粗

设置了格式: 字体: 加粗

设置了格式: 字体: 加粗

设置了格式: 字体: 加粗

带格式的: 两端对齐, 缩进: 首行缩进: 0 厘米, 左 0 字符



673
 674 **Figure 11.** A schematic diagram of the transportation of air pollutants and ageing
 675 process from the YRD city cluster to Yangzhou during the 2021 summer COVID-19
 676 lockdown.

带格式的: 正文, 段落间距段后: 0 磅

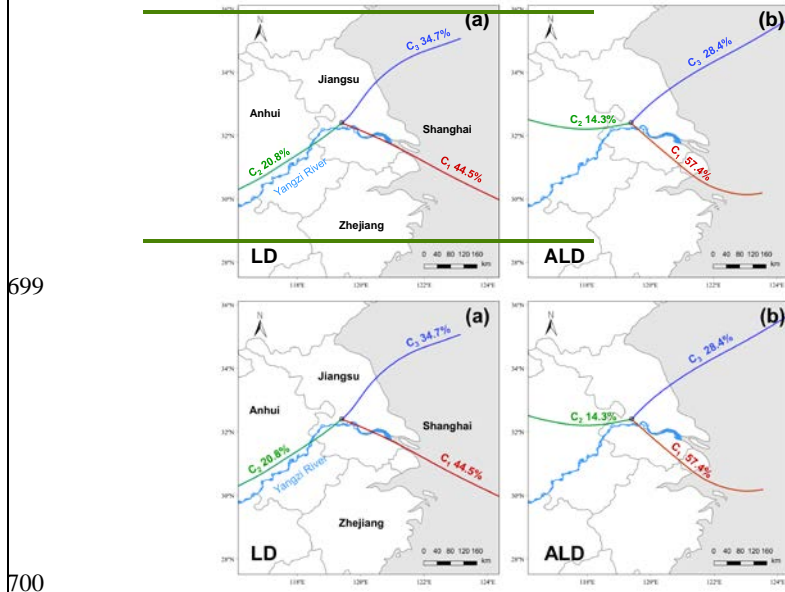
677 4.13 Local and non-local source analysis

678 Since there was a heavy precipitation on July 28th (the day before lockdown) which
 679 removed most atmospheric pollutants, the air pollutants might be influenced mostly by
 680 regional transport as local emissions were significantly cut down during the LD period.
 681 As a comparison, the pollution during the ALD period might be caused by both local
 682 emissions and regional transport. Additionally, the meteorological conditions were
 683 relatively stable during the LD and ALD periods (Figure 2a-e); the trajectories of these
 684 two periods were both categorized into similar 3 clusters, indicating stable regional
 685 transport of the pollutants from the southeast, southwest, and northeast (Figure 12). The
 686 lockdown event with favorable meteorological conditions provided a valuable
 687 opportunity to investigate emissions-meteorology interactions in YRD during summer.
 688 Here, we propose a method to roughly estimate the local and non-local proportions of
 689 for each type of BCc particles in Yangzhou during the ALD period (representing the
 690 usual emission condition)

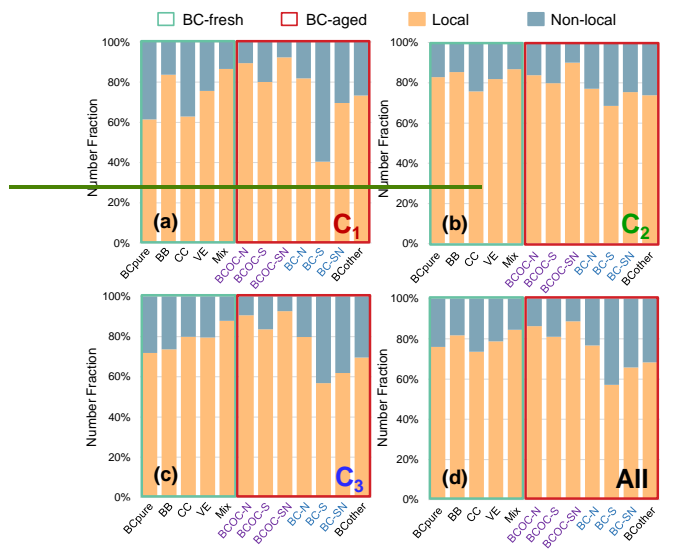
691
$$[PM]_{i,j}^{non-local} = [PM]_{i,j}^{LD} \times t_i^{ALD} / t_i^{LD}; \quad (4)$$

692
$$[PM]_{i,j}^{local} = [PM]_{i,j}^{ALD} - [PM]_{i,j}^{non-local}. \quad (5)$$

693 For Equation (4-5), the duration of the i^{th} cluster in different periods is represented by
 694 t_i^{LD} and t_i^{ALD} . The sum of the hourly number density of the j^{th} type of particulate matter
 695 in the i^{th} cluster during the LD period is denoted as $[PM]_{i,j}^{LD}$. Similarly, $[PM]_{i,j}^{non-local}$
 696 and $[PM]_{i,j}^{local}$ indicate the summed hourly number density of specific types of BCe
 697 particles from non local and local sources in the i^{th} cluster during the ALD period,
 698 respectively.



700
 701 **Figure 12.** Back trajectory analysis during (a) LD and (b) ALD period. The
 702 corresponding percentages of total trajectories for Cluster1 (C₁, red), Cluster2 (C₂,
 703 green) and Cluster3 (C₃, blue) are also shown.



704 **Figure 13.** Number fraction of local and non local in different types of particles in (a)
 705 Cluster1 (C₁), (b) Cluster2 (C₂), (c) Cluster3 (C₃), and (d) all clusters during the ALD
 706 period. The purple labels represent BCOc particles and the blue labels represent BC-
 707 SNA particles.
 708

709
 710 By using this method, analysis results of the sources of all types of BCe particles from
 711 different clusters are presented in Figure 13a-c. Cluster1 (C₁), originating from the
 712 economically developed southeast region, accounted for 57.4% of total trajectories
 713 during the ALD period. C₁ exhibited the highest proportions of non local fresh BCe
 714 (BC pure, 38.6%) and coal combustion BCe (CC 37.1%), along with vehicular ones
 715 (VE 24.3%), underscoring the substantial impact of heavy industry and transportation
 716 from the southeastern YRD during summer (Figure 13b). Notably, non local
 717 contribution of BC S was dominant in C₁, indicating significant regionally transported
 718 sulfate. Cluster2 (C₂), originating from the southwest region covering Nanjing and
 719 eastern Anhui province, accounted for 14.3% of all trajectories (Figure 12b). The non-
 720 local proportions for all particle types were around 20%, indicating that local emission
 721 was dominant (Figure 13b). Cluster 3 (C₃), originating from the East China Sea and
 722 passing through the vast cultivated area in northeastern Jiangsu Province, contributed
 723 28.4% of the total trajectories (Figure 12b). A relatively high proportion of BCe
 724 particles generated by non local biomass burning emissions (BB, 26.4%) was observed
 725 in C₃, indicating a correlation between BCe particles from the northeastern YRD and
 726 open field burning of agricultural residues during summer (Figure 13c).

727
 728 Regarding the number fraction of local and non local contributions for the whole
 729 campaign (Figure 13d), the proportion of local BC N particles (~80%) exceeded that
 730 of BC S (~60%; note non local contribution of BC S even dominated over local

731 counterpart in C_1), suggesting that sulfate-associated BCe particles were more likely
732 from regional transport than those of nitrate associated ones. The proportion of non-
733 local BC aged particles was relatively higher than the BC fresh particles naturally, as
734 BC aged particles intercepted more secondary species during the regional transport
735 than freshly emitted BCe particles. Furthermore, the proportion of local BCOC particles
736 exceeded that of BC-SNA particles, implying a strong relationship between BCOC
737 particles and local emission, whereas more BC-SNA particles were likely associated
738 with regional transport. Overall, BCe particles was predominantly local (78%) in
739 Yangzhou during normal summertime. However, BCe particle from coal combustion
740 (CC, 26%) and vehicle emission (VE, 21%) transported from the southeast, as well as
741 biomass burning related emissions (BB, 19%) from the northeast, were also significant
742 contributors that should not be ignored (Figure 13d). These findings highlight the
743 importance of considering both local and regional sources, as well as understanding the
744 transport characteristics of different types of BCe particles for air quality management.

745 **5.4. Conclusions and implications**

746 During the summer of 2021, the COVID-19 lockdown imposed in Yangzhou resulted
747 in a significant decrease in anthropogenic emissions from traffic and manufacturing
748 sectors. To examine the effects of this lockdown, we utilized spaceborne observations,
749 ground-based measurements, and particularly SPA-MS analysis to explore the
750 variations, aging characteristics, and sources of BCc in the YRD. We showed that the
751 strict emission controls effectively reduced local gaseous pollutants. However, the
752 decline in NO_x (-30.1%) and TVOC (-5.3%) levels might on the other hand result in
753 increased ~~ozone~~ O_3 (+19.9%), leading to a rise in BC-aged particles and a slight
754 elevation in $\text{PM}_{2.5}$ levels during the lockdown. Our results revealed a strong non-linear
755 response of $\text{PM}_{2.5}$ and O_3 to the gaseous precursors.

756
757 The SPA-MS analysis results further demonstrate significant enhancement of OM and
758 SNA coating species on BC-fresh particles, owing to gas-to-particle partitioning and
759 nocturnal multiphase chemistry. Consequently, we observed a higher fraction of BC-
760 aged particles (73%) during the lockdown due to enhanced oxidizing capacity and high
761 relative humidity ($\text{RH} > 85\%$). The BC-fresh particles tended to mix with SNA under
762 high RH conditions, while high TVOC levels were accompanied by BCOC formation.
763 However, BCOC particles generally exhibited smaller sizes compared to BC-SNA
764 particles. Moreover, we ~~postulate-propose~~ that aqueous or heterogeneous reactions
765 might be important to generate BCOC and BC-SNA particles, especially ones with
766 ~ 400 nm D_{va} , while coagulation might play a more prominent role in larger BC-aged
767 particles. The aging process during LD promoted the conversion of partly coated
768 particles to totally coated ones, with larger diameters (~ 600 nm) and thicker coatings.

769
770 ~~Furthermore, our study highlights that local emissions were the main source of BCe~~
771 ~~particles in Yangzhou during normal summertime. However, regional transported coal~~

设置了格式: 下标

设置了格式: 非突出显示

772 combustion (23%) and vehicle emissions (21%) from southeast, as well as biomass
773 burning emissions (19%) from the northeast, were also significant. Meteorological
774 conditions, including wind patterns and relative humidity, also influenced the regional
775 transport of BCe particles in the YRD.

776

777 It should be noted that the observed average PM_{2.5} concentration during the lockdown
778 in Yangzhou was 21.2 μg m⁻³, which still significantly exceeds the WHO's air quality
779 guideline of 5 μg m⁻³. Our research underscores the crucial role of BCc, which
780 constitutes a significant portion of PM_{2.5}, in particulate matter pollution. These particles
781 originate from diverse combustion sources and their behavior is intricately influenced
782 by complex chemistry, regional transport, and meteorological factors. Mere reductions
783 in local primary emissions from traffic and manufacturing sectors exhibit limited
784 efficacy in air quality improvement. Therefore, effective air quality remediation
785 strategies necessitate nuanced control of BCc alongside broader emission reduction
786 efforts. Our research highlights that reduction of local primary emissions from traffic
787 and manufacturing sectors alone has limited effect in air quality remediation. Complex
788 chemistry, regional transport and meteorological factors need to be considered
789 cooperatively. Therefore, we suggest a more comprehensive regulation of precursor
790 gases from multiple sectors, a wide-ranging joint regulation approach as well as proper
791 consideration of the chemistry, to develop an effective strategy for air quality
792 improvement.

793

设置了格式: 字体: 非倾斜, 突出显示

设置了格式: 突出显示

设置了格式: 字体: 非倾斜, 突出显示

设置了格式: 突出显示

设置了格式: 字体: 非倾斜, 突出显示

设置了格式: 突出显示

设置了格式: 字体: 非倾斜, 突出显示

设置了格式: 突出显示

794

795 **Data availability.** The data in this study are available from the corresponding author
796 upon request (caxinra@163.com).

797

798 **Author contributions.** XG, JW, and YD designed the research. YD, HW, and SC
799 conducted the field measurements. YD, HW, JW, and SC analyzed the data. XG, JW,
800 HL, YW, YZ, and EA reviewed the paper and provided useful suggestions. YD, JW,
801 and XG wrote the first draft of the paper. All people were involved in the discussion of
802 the results.

803

804 **Supplement.** The supplement related to this article is available online at XXX.

805

806 **Competing interests.** The contact author has declared that neither they nor their co-
807 authors have any competing interests.

808

809 **Financial support.** This research has been supported by the National Natural Science
810 Foundation of China (grant nos. 42377100, 22276099, and 42021004).

811 **References**

- 812 Adachi, K., Zaizen, Y., Kajino, M., Igarashi, Y., 2014. Mixing state of regionally
813 transported soot particles and the coating effect on their size and shape at a
814 mountain site in Japan. *Journal of Geophysical Research: Atmospheres* 119,
815 5386–5396. <https://doi.org/10.1002/2013JD020880>
- 816 Benedetti, A., Morcrette, J.-J., Boucher, O., Dethof, A., Engelen, R.J., Fisher, M.,
817 Flentje, H., Huneeus, N., Jones, L., Kaiser, J.W., Kinne, S., Mangold, A.,
818 Razingert, M., Simmons, A.J., Suttie, M., 2009. Aerosol analysis and forecast in
819 the European Centre for Medium-Range Weather Forecasts Integrated Forecast
820 System: 2. Data assimilation. *Journal of Geophysical Research: Atmospheres*
821 114. <https://doi.org/10.1029/2008JD011115>
- 822 Bond, T.C., Bergstrom, R.W., 2006. Light Absorption by Carbonaceous Particles: An
823 Investigative Review. *Aerosol Science and Technology* 40, 27–67.
824 <https://doi.org/10.1080/02786820500421521>
- 825 Bond, T.C., Doherty, S., Fahey, D.W., Forster, P., Berntsen, T., DeAngelo, B., Flanner,
826 M., Ghan, S., Kärcher, B., Koch, D., Kinne, S., Kondo, Y., Quinn, P.K., Sarofim,
827 M., Schultz, M., Michael, S., Venkataraman, C., Zhang, H., Zhang, S., Zender,
828 C.S., 2013. Bounding the role of black carbon in the climate system: A Scientific
829 assessment. *Journal of Geophysical Research: Atmospheres* 118, 5380–5552.
830 <https://doi.org/10.1002/jgrd.50171>
- 831 Cappa, C.D., Zhang, X., Russell, L.M., Collier, S., Lee, A.K.Y., Chen, C.-L., Betha, R.,
832 Chen, S., Liu, J., Price, D.J., Sanchez, K.J., McMeeking, G.R., Williams, L.R.,
833 Onasch, T.B., Worsnop, D.R., Abbatt, J., Zhang, Q., 2019. Light Absorption by
834 Ambient Black and Brown Carbon and its Dependence on Black Carbon
835 Coating State for Two California, USA, Cities in Winter and Summer. *Journal*
836 *of Geophysical Research: Atmospheres* 124, 1550–1577.
837 <https://doi.org/10.1029/2018JD029501>
- 838 Chang, Y., Huang, R., Ge, X., Huang, X., Hu, J., Duan, Y., Zou, Z., Liu, X., Lehmann,
839 M.F., 2020. Puzzling Haze Events in China During the Coronavirus (COVID-
840 19) Shutdown. *Geophys. Res. Lett.* 47. <https://doi.org/10.1029/2020GL088533>
- 841 Chen, H., Huo, J., Fu, Q., Duan, Y., Xiao, H., Chen, J., 2020. Impact of quarantine
842 measures on chemical compositions of PM_{2.5} during the COVID-19 epidemic
843 in Shanghai, China. *Science of The Total Environment* 743, 140758.
844 <https://doi.org/10.1016/j.scitotenv.2020.140758>
- 845 Chen, L., Qi, X., Nie, W., Wang, J., Xu, Zheng, Wang, T., Liu, Y., Shen, Y., Xu,
846 Zhengning, Kokkonen, T., Chi, X., Aalto, P., Paasonen, P., Kerminen, V.-M.,
847 Petäjä, T., Kulmala, M., Ding, A., 2021. Cluster Analysis of Submicron Particle
848 Number Size Distributions at the SORPES Station in the Yangtze River Delta
849 of East China. *Journal of Geophysical Research: Atmospheres* 126.
850 <https://doi.org/10.1029/2020JD034004>
- 851 Chen, L., Zhang, F., Yan, P., Wang, X., Sun, L., Li, Y., Zhang, X., Sun, Y., Li, Z., 2020.
852 The large proportion of black carbon (BC)-containing aerosols in the urban

853 atmosphere. *Environmental Pollution* 263, 114507.
854 <https://doi.org/10.1016/j.envpol.2020.114507>

855 Cheng, Y.F., Su, H., Rose, D., Gunthe, S.S., Berghof, M., Wehner, B., Achtert, P.,
856 Nowak, A., Takegawa, N., Kondo, Y., Shiraiwa, M., Gong, Y.G., Shao, M., Hu,
857 M., Zhu, T., Zhang, Y.H., Carmichael, G.R., Wiedensohler, A., Andreae, M.O.,
858 Pöschl, U., 2012. Size-resolved measurement of the mixing state of soot in the
859 megacity Beijing, China: diurnal cycle, aging and parameterization.
860 *Atmospheric Chemistry and Physics* 12, 4477–4491.
861 <https://doi.org/10.5194/acp-12-4477-2012>

862 Chien, L.-C., Chen, L.-W.A., Lin, R.-T., 2022. Lagged meteorological impacts on
863 COVID-19 incidence among high-risk counties in the United States—a
864 spatiotemporal analysis. *J Expo Sci Environ Epidemiol* 32, 774–781.
865 <https://doi.org/10.1038/s41370-021-00356-y>

866 Clemente, Á., Yubero, E., Nicolás, J.F., Caballero, S., Crespo, J., Galindo, N., 2022.
867 Changes in the concentration and composition of urban aerosols during the
868 COVID-19 lockdown. *Environmental Research* 203, 111788.
869 <https://doi.org/10.1016/j.envres.2021.111788>

870 Cui, S., Xian, J., Shen, F., Zhang, L., Deng, B., Zhang, Y., Ge, X., 2021. One-Year Real-
871 Time Measurement of Black Carbon in the Rural Area of Qingdao, Northeastern
872 China: Seasonal Variations, Meteorological Effects, and the COVID-19 Case
873 Analysis. *Atmosphere* 12, 394. <https://doi.org/10.3390/atmos12030394>

874 Cui, Y., Ji, D., Maenhaut, W., Gao, W., Zhang, R., Wang, Y., 2020. Levels and sources
875 of hourly PM_{2.5}-related elements during the control period of the COVID-19
876 pandemic at a rural site between Beijing and Tianjin. *Science of The Total
877 Environment* 744, 140840. <https://doi.org/10.1016/j.scitotenv.2020.140840>

878 Ding, A., Huang, X., Nie, W., Chi, X., Xu, Zheng, Zheng, L., Xu, Zhengning, Xie, Y.,
879 Qi, X., Shen, Y., Sun, P., Wang, J., Wang, L., Sun, J., Yang, X.-Q., Qin, W.,
880 Zhang, X., Cheng, W., Liu, W., Pan, L., Fu, C., 2019. Significant reduction of
881 PM_{2.5} in eastern China due to regional-scale emission control: evidence from
882 SORPES in 2011–2018. *Atmospheric Chemistry and Physics* 19, 11791–11801.
883 <https://doi.org/10.5194/acp-19-11791-2019>

884 Ding, S., Liu, D., Hu, K., Zhao, D., Tian, P., Wang, F., Li, R., Chen, Y., He, H., Huang,
885 M., Ding, D., 2021. Optical and hygroscopic properties of black carbon
886 influenced by particle microphysics at the top of the anthropogenically polluted
887 boundary layer. *Atmospheric Chemistry & Physics* 21, 681–694.
888 <https://doi.org/10.5194/acp-21-681-2021>

889 Feng, Z., Zheng, F., Liu, Y., Fan, X., Yan, C., Zhang, Y., Daellenbach, K.R., Bianchi, F.,
890 Petäjä, T., Kulmala, M., Bao, X., 2022. Evolution of organic carbon during
891 COVID-19 lockdown period: Possible contribution of nocturnal chemistry. *Sci
892 Total Environ* 808, 152191. <https://doi.org/10.1016/j.scitotenv.2021.152191>

893 Ge, B., Xu, D., Wild, O., Yao, X., Wang, J., Chen, X., Qixin, T., Pan, X., Wang, Z.,
894 2020. Inter-annual variations of wet deposition in Beijing during 2014–2017:

895 implications of below-cloud scavenging of inorganic aerosols.
896 <https://doi.org/10.5194/acp-2020-1146>

897 Gorelick, N., Hancher, M., Dixon, M., Ilyushchenko, S., Thau, D., Moore, R., 2017.
898 Google Earth Engine: Planetary-scale geospatial analysis for everyone. *Remote*
899 *Sensing of Environment, Big Remotely Sensed Data: tools, applications and*
900 *experiences* 202, 18–27. <https://doi.org/10.1016/j.rse.2017.06.031>

901 He, C., Liou, K.-N., Takano, Y., Zhang, R., Levy Zamora, M., Yang, P., Li, Q., Leung,
902 L.R., 2015. Variation of the radiative properties during black carbon aging:
903 theoretical and experimental intercomparison. *Atmospheric Chemistry and*
904 *Physics* 15, 11967–11980. <https://doi.org/10.5194/acp-15-11967-2015>

905 Hopke, P.K., Gao, N., Cheng, M.-D., 1993. Combining chemical and meteorological
906 data to infer source areas of airborne pollutants. *Chemometrics and Intelligent*
907 *Laboratory Systems, Proceedings of the 5th Conference on Computer*
908 *Applications in Analytical Chemistry (COMPANA '92)* 19, 187–199.
909 [https://doi.org/10.1016/0169-7439\(93\)80103-O](https://doi.org/10.1016/0169-7439(93)80103-O)

910 Huang, X., Ding, A., Gao, J., Zheng, B., Zhou, D., Qi, X., Tang, R., Wang, J., Ren, C.,
911 Nie, W., Chi, X., Xu, Z., Chen, L., Li, Y., Che, F., Pang, N., Wang, H., Tong, D.,
912 Qin, W., Cheng, W., Liu, W., Fu, Q., Liu, B., Chai, F., Davis, S.J., Zhang, Q.,
913 He, K., 2021. Enhanced secondary pollution offset reduction of primary
914 emissions during COVID-19 lockdown in China. *Natl Sci Rev* 8, nwaal37.
915 <https://doi.org/10.1093/nsr/nwaal37>

916 Huang, X., Wang, Z., Ding, A., 2018. Impact of Aerosol-PBL Interaction on Haze
917 Pollution: Multiyear Observational Evidences in North China. *Geophysical*
918 *Research Letters* 45, 8596–8603. <https://doi.org/10.1029/2018GL079239>

919 Isokääntä, S., Kim, P., Mikkonen, S., Kühn, T., Kokkola, H., Yli-Juuti, T., Heikkinen,
920 L., Luoma, K., Petäjä, T., Kipling, Z., Partridge, D., Virtanen, A., 2022. The
921 effect of clouds and precipitation on the aerosol concentrations and composition
922 in a boreal forest environment. *Atmospheric Chemistry and Physics* 22, 11823–
923 11843. <https://doi.org/10.5194/acp-22-11823-2022>

924 Jacobson, M.Z., 2002. Analysis of aerosol interactions with numerical techniques for
925 solving coagulation, nucleation, condensation, dissolution, and reversible
926 chemistry among multiple size distributions. *Journal of Geophysical Research:*
927 *Atmospheres* 107, AAC 2-1-AAC 2-23. <https://doi.org/10.1029/2001JD002044>

928 Jain, C.D., Madhavan, B.L., Singh, V., Prasad, P., Sai Krishnaveni, A., Ravi Kiran, V.,
929 Venkat Ratnam, M., 2021. Phase-wise analysis of the COVID-19 lockdown
930 impact on aerosol, radiation and trace gases and associated chemistry in a
931 tropical rural environment. *Environmental Research* 194, 110665.
932 <https://doi.org/10.1016/j.envres.2020.110665>

933 Jeong, C.-H., Yousif, M., Evans, G.J., 2022. Impact of the COVID-19 lockdown on the
934 chemical composition and sources of urban PM2.5. *Environmental Pollution*
935 292, 118417. <https://doi.org/10.1016/j.envpol.2021.118417>

936 Kahnert, M., 2010. On the Discrepancy between Modeled and Measured Mass

937 Absorption Cross Sections of Light Absorbing Carbon Aerosols. *Aerosol*
938 *Science and Technology* 44, 453–460.
939 <https://doi.org/10.1080/02786821003733834>

940 Kandler, K., Schneiders, K., Ebert, M., Hartmann, M., Weinbruch, S., Prass, M.,
941 Pöhlker, C., 2018. Composition and mixing state of atmospheric aerosols
942 determined by electron microscopy: method development and application to
943 aged Saharan dust deposition in the Caribbean boundary layer. *Atmospheric*
944 *Chemistry and Physics* 18, 13429–13455. [https://doi.org/10.5194/acp-18-](https://doi.org/10.5194/acp-18-13429-2018)
945 [13429-2018](https://doi.org/10.5194/acp-18-13429-2018)

946 Kondo, Y., Matsui, H., Moteki, N., Sahu, L., Takegawa, N., Kajino, M., Zhao, Y.,
947 Cubison, M.J., Jimenez, J.L., Vay, S., Diskin, G.S., Anderson, B., Wisthaler, A.,
948 Mikoviny, T., Fuelberg, H.E., Blake, D.R., Huey, G., Weinheimer, A.J., Knapp,
949 D.J., Brune, W.H., 2011. Emissions of black carbon, organic, and inorganic
950 aerosols from biomass burning in North America and Asia in 2008. *Journal of*
951 *Geophysical Research: Atmospheres* 116.
952 <https://doi.org/10.1029/2010JD015152>

953 Laughner, J.L., Neu, J.L., Schimel, D., Wennberg, P.O., Barsanti, K., Bowman, K.W.,
954 Chatterjee, A., Croes, B.E., Fitzmaurice, H.L., Henze, D.K., Kim, J., Kort, E.A.,
955 Liu, Z., Miyazaki, K., Turner, A.J., Anenberg, S., Avise, J., Cao, H., Crisp, D.,
956 de Gouw, J., Eldering, A., Fyfe, J.C., Goldberg, D.L., Gurney, K.R.,
957 Hasheminassab, S., Hopkins, F., Ivey, C.E., Jones, D.B.A., Liu, J., Lovenduski,
958 N.S., Martin, R.V., McKinley, G.A., Ott, L., Poulter, B., Ru, M., Sander, S.P.,
959 Swart, N., Yung, Y.L., Zeng, Z.-C., 2021. Societal shifts due to COVID-19
960 reveal large-scale complexities and feedbacks between atmospheric chemistry
961 and climate change. *Proc Natl Acad Sci U S A* 118, e2109481118.
962 <https://doi.org/10.1073/pnas.2109481118>

963 Le, T., Wang, Y., Liu, L., Yang, J., Yung, Y.L., Li, G., Seinfeld, J.H., 2020. Unexpected
964 air pollution with marked emission reductions during the COVID-19 outbreak
965 in China. *Science* 369, 702–706. <https://doi.org/10.1126/science.abb7431>

966 Li, J., Jiang, L., Chen, C., Liu, D., Du, S., Zhang, Y., Yang, Y., Tang, L., 2020.
967 Characteristics and Sources of Black Carbon Aerosol in a Mega-City in the
968 Western Yangtze River Delta, China. *Atmosphere* 11, 315.
969 <https://doi.org/10.3390/atmos11040315>

970 Li, K., Wang, X., Lu, X., Chen, H., Yang, X., 2022. Effects of Volatile Components on
971 Mixing State and Size Distribution of Individual Black Carbon Aerosols.
972 *Aerosol Air Qual. Res.* 22, 210400. <https://doi.org/10.4209/aaqr.210400>

973 Li, L., Huang, Z., Dong, J., Li, M., Gao, W., Nian, H., Fu, Z., Zhang, G., Bi, X., Cheng,
974 P., Zhou, Z., 2011. Real time bipolar time-of-flight mass spectrometer for
975 analyzing single aerosol particles. *International Journal of Mass Spectrometry*
976 303, 118–124. <https://doi.org/10.1016/j.ijms.2011.01.017>

977 Li, L., Li, Q., Huang, L., Wang, Q., Zhu, A., Xu, J., Liu, Ziyi, Li, H., Shi, L., Li, R.,
978 Azari, M., Wang, Y., Zhang, X., Liu, Zhiqiang, Zhu, Y., Zhang, K., Xue, S., Ooi,

979 M.C.G., Zhang, D., Chan, A., 2020. Air quality changes during the COVID-19
980 lockdown over the Yangtze River Delta Region: An insight into the impact of
981 human activity pattern changes on air pollution variation. *Science of The Total*
982 *Environment* 732, 139282. <https://doi.org/10.1016/j.scitotenv.2020.139282>

983 Liu, D., Joshi, R., Wang, J., Yu, C., Allan, J.D., Coe, H., Flynn, M.J., Xie, C., Lee, J.,
984 Squires, F., Kotthaus, S., Grimmond, S., Ge, X., Sun, Y., Fu, P., 2019.
985 Contrasting physical properties of black carbon in urban Beijing between winter
986 and summer. *Atmospheric Chemistry and Physics* 19, 6749–6769.
987 <https://doi.org/10.5194/acp-19-6749-2019>

988 Liu, Q., Jing, B., Peng, C., Tong, S., Wang, W., Ge, M., 2016. Hygroscopicity of
989 internally mixed multi-component aerosol particles of atmospheric relevance.
990 *Atmospheric Environment* 125, 69–77.
991 <https://doi.org/10.1016/j.atmosenv.2015.11.003>

992 Luo, J., Li, Z., Zhang, C., Zhang, Q., Zhang, Yongming, Zhang, Ying, Curci, G.,
993 Chakrabarty, R.K., 2022. Regional impacts of black carbon morphologies on
994 shortwave aerosol–radiation interactions: a comparative study between the US
995 and China. *Atmospheric Chemistry and Physics* 22, 7647–7666.
996 <https://doi.org/10.5194/acp-22-7647-2022>

997 Moffet, R.C., Rödel, T.C., Kelly, S.T., Yu, X.Y., Carroll, G.T., Fast, J., Zaveri, R.A.,
998 Laskin, A., Gilles, M.K., 2013. Spectro-microscopic measurements of
999 carbonaceous aerosol aging in Central California. *Atmospheric Chemistry and*
1000 *Physics* 13, 10445–10459. <https://doi.org/10.5194/acp-13-10445-2013>

1001 Morcrette, J.-J., Boucher, O., Jones, L., Salmond, D., Bechtold, P., Beljaars, A.,
1002 Benedetti, A., Bonet, A., Kaiser, J.W., Razinger, M., Schulz, M., Serrar, S.,
1003 Simmons, A.J., Sofiev, M., Suttie, M., Tompkins, A.M., Untch, A., 2009.
1004 Aerosol analysis and forecast in the European Centre for Medium-Range
1005 Weather Forecasts Integrated Forecast System: Forward modeling. *Journal of*
1006 *Geophysical Research: Atmospheres* 114.
1007 <https://doi.org/10.1029/2008JD011235>

1008 Nie, D., Shen, F., Wang, J., Ma, X., Li, Z., Ge, P., Ou, Y., Jiang, Y., Chen, Meijuan,
1009 Chen, Mindong, Wang, T., Ge, X., 2021. Changes of air quality and its
1010 associated health and economic burden in 31 provincial capital cities in China
1011 during COVID-19 pandemic. *Atmos Res* 249, 105328.
1012 <https://doi.org/10.1016/j.atmosres.2020.105328>

1013 Peng, J., Hu, M., Guo, S., Du, Z., Zheng, Jing, Shang, D., Levy Zamora, M., Zeng, L.,
1014 Shao, M., Wu, Y.-S., Zheng, Jun, Wang, Y., Glen, C.R., Collins, D.R., Molina,
1015 M.J., Zhang, R., 2016. Markedly enhanced absorption and direct radiative
1016 forcing of black carbon under polluted urban environments. *Proceedings of the*
1017 *National Academy of Sciences* 113, 4266–4271.
1018 <https://doi.org/10.1073/pnas.1602310113>

1019 Polissar, A.V., Hopke, P.K., Paatero, P., Kaufmann, Y.J., Hall, D.K., Bodhaine, B.A.,
1020 Dutton, E.G., Harris, J.M., 1999. The aerosol at Barrow, Alaska: long-term

1021 trends and source locations. *Atmospheric Environment* 33, 2441–2458.
1022 [https://doi.org/10.1016/S1352-2310\(98\)00423-3](https://doi.org/10.1016/S1352-2310(98)00423-3)

1023 Qin, M., Hu, A., Mao, J., Li, X., Sheng, L., Sun, J., Li, J., Wang, X., Zhang, Y., Hu, J.,
1024 2021. PM_{2.5} and O₃ relationships affected by the atmospheric oxidizing
1025 capacity in the Yangtze River Delta, China. *Science of The Total Environment*
1026 152268. <https://doi.org/10.1016/j.scitotenv.2021.152268>

1027 Ramanathan, V., Carmichael, G., 2008. Global and regional climate changes due to
1028 black carbon. *Nature Geoscience* 1, 221–227. <https://doi.org/10.1038/ngeo156>

1029 Sedlacek, A.J., Lewis, E.R., Onasch, T.B., Zuidema, P., Redemann, J., Jaffe, D.,
1030 Kleinman, L.I., 2022. Using the Black Carbon Particle Mixing State to
1031 Characterize the Lifecycle of Biomass Burning Aerosols. *Environ. Sci. Technol.*
1032 56, 14315–14325. <https://doi.org/10.1021/acs.est.2c03851>

1033 Silva, P.J., Liu, D.-Y., Noble, C.A., Prather, K.A., 1999. Size and Chemical
1034 Characterization of Individual Particles Resulting from Biomass Burning of
1035 Local Southern California Species. *Environ. Sci. Technol.* 33, 3068–3076.
1036 <https://doi.org/10.1021/es980544p>

1037 Song, X.-H., Hopke, P.K., Fergenson, D.P., Prather, K.A., 1999. Classification of Single
1038 Particles Analyzed by ATOFMS Using an Artificial Neural Network, ART-2A.
1039 *Anal. Chem.* 71, 860–865. <https://doi.org/10.1021/ac9809682>

1040 Steinfeld, J.I., 1998. *Atmospheric Chemistry and Physics: From Air Pollution to*
1041 *Climate Change. Environment: Science and Policy for Sustainable*
1042 *Development* 40, 26–26. <https://doi.org/10.1080/00139157.1999.10544295>

1043 Sulaymon, I.D., Zhang, Yuanxun, Hopke, P.K., Hu, J., Zhang, Yang, Li, L., Mei, X.,
1044 Gong, K., Shi, Z., Zhao, B., Zhao, F., 2021a. Persistent high PM_{2.5} pollution
1045 driven by unfavorable meteorological conditions during the COVID-19
1046 lockdown period in the Beijing-Tianjin-Hebei region, China. *Environmental*
1047 *Research* 198, 111186. <https://doi.org/10.1016/j.envres.2021.111186>

1048 Sulaymon, I.D., Zhang, Yuanxun, Hopke, P.K., Zhang, Yang, Hua, J., Mei, X., 2021b.
1049 COVID-19 pandemic in Wuhan: Ambient air quality and the relationships
1050 between criteria air pollutants and meteorological variables before, during, and
1051 after lockdown. *Atmospheric Research* 250, 105362.
1052 <https://doi.org/10.1016/j.atmosres.2020.105362>

1053 Sun, J., Sun, Y., Xie, C., Xu, Weiqi, Chen, C., Wang, Zhe, Li, L., Du, X., Huang, F., Li,
1054 Y., Li, Z., Pan, X., Ma, N., Xu, Wanyun, Fu, P., Wang, Zifa, 2022. The chemical
1055 composition and mixing state of BC-containing particles and the implications
1056 on light absorption enhancement. *Atmos. Chem. Phys.* 22, 7619–7630.
1057 <https://doi.org/10.5194/acp-22-7619-2022>

1058 Sun, J., Wang, Zhe, Zhou, W., Xie, C., Wu, C., Chen, C., Han, T., Wang, Q., Li, Z., Li,
1059 J., Fu, P., Wang, Zifa, Sun, Y., 2021. Measurement report: Long-term changes
1060 in black carbon and aerosol optical properties from 2012 to 2020 in Beijing,
1061 China (preprint). *Aerosols/Field Measurements/Troposphere/Physics (physical*
1062 *properties and processes)*. <https://doi.org/10.5194/acp-2021-637>

- 1063 Sun, Y., Du, W., Fu, P., Wang, Q., Li, J., Ge, X., Zhang, Q., Zhu, C., Ren, L., Xu, W.,
1064 Zhao, J., Han, T., Worsnop, D.R., Wang, Z., 2016. Primary and secondary
1065 aerosols in Beijing in winter: sources, variations and processes. *Atmos. Chem.*
1066 *Phys.*
- 1067 Sun, Y., Lei, L., Zhou, W., Chen, C., He, Y., Sun, J., Li, Z., Xu, W., Wang, Q., Ji, D., Fu,
1068 P., Wang, Z., Worsnop, D.R., 2020. A chemical cocktail during the COVID-19
1069 outbreak in Beijing, China: Insights from six-year aerosol particle composition
1070 measurements during the Chinese New Year holiday. *Science of The Total*
1071 *Environment* 742, 140739. <https://doi.org/10.1016/j.scitotenv.2020.140739>
- 1072 Taylor, J.W., Allan, J.D., Allen, G., Coe, H., Williams, P.I., Flynn, M.J., Le Breton, M.,
1073 Muller, J.B.A., Percival, C.J., Oram, D., Forster, G., Lee, J.D., Rickard, A.R.,
1074 Parrington, M., Palmer, P.I., 2014. Size-dependent wet removal of black carbon
1075 in Canadian biomass burning plumes. *Atmospheric Chemistry and Physics* 14,
1076 13755–13771. <https://doi.org/10.5194/acp-14-13755-2014>
- 1077 Wang, H., Miao, Q., Shen, L., Yang, Q., Wu, Y., Wei, H., 2021. Air pollutant variations
1078 in Suzhou during the 2019 novel coronavirus (COVID-19) lockdown of 2020:
1079 High time-resolution measurements of aerosol chemical compositions and
1080 source apportionment. *Environmental Pollution* 271, 116298.
1081 <https://doi.org/10.1016/j.envpol.2020.116298>
- 1082 Wang, J., Ge, X., Sonya, C., Ye, J., Lei, Y., Chen, M., Zhang, Q., 2022. Influence of
1083 regional emission controls on the chemical composition, sources, and size
1084 distributions of submicron aerosols: Insights from the 2014 Nanjing Youth
1085 Olympic Games. *Science of The Total Environment* 807, 150869.
1086 <https://doi.org/10.1016/j.scitotenv.2021.150869>
- 1087 Wang, J., Liu, D., Ge, X., Wu, Y., Shen, F., Chen, M., Zhao, J., Xie, C., Wang, Q., Xu,
1088 W., Zhang, J., Hu, J., Allan, J., Joshi, R., Fu, P., Coe, H., Sun, Y., 2019.
1089 Characterization of black carbon-containing fine particles in Beijing during
1090 wintertime. *Atmos. Chem. Phys.* 19, 447–458. [https://doi.org/10.5194/acp-19-](https://doi.org/10.5194/acp-19-447-2019)
1091 [447-2019](https://doi.org/10.5194/acp-19-447-2019)
- 1092 Wang, Pengfei, Chen, K., Zhu, S., Wang, Peng, Zhang, H., 2020. Severe air pollution
1093 events not avoided by reduced anthropogenic activities during COVID-19
1094 outbreak. *Resources, Conservation and Recycling* 158, 104814.
1095 <https://doi.org/10.1016/j.resconrec.2020.104814>
- 1096 Wang, Q., Liu, S., Zhou, Y., Cao, J., Han, Y., Ni, H., Zhang, N., Huang, R., 2015.
1097 Characteristics of Black Carbon Aerosol during the Chinese Lunar Year and
1098 Weekdays in Xi'an, China. *Atmosphere* 6, 195–208.
1099 <https://doi.org/10.3390/atmos6020195>
- 1100 Wang, S., Zhao, M., Xing, J., Wu, Y., Zhou, Y., Lei, Y., He, K., Fu, L., Hao, J., 2010.
1101 Quantifying the Air Pollutants Emission Reduction during the 2008 Olympic
1102 Games in Beijing. *Environ. Sci. Technol.* 44, 2490–2496.
1103 <https://doi.org/10.1021/es9028167>
- 1104 Wang, Y., Zhu, S., Ma, J., Shen, J., Wang, Pengfei, Wang, Peng, Zhang, H., 2021.

1105 Enhanced atmospheric oxidation capacity and associated ozone increases
 1106 during COVID-19 lockdown in the Yangtze River Delta. *Science of The Total*
 1107 *Environment* 768, 144796. <https://doi.org/10.1016/j.scitotenv.2020.144796>
 1108 Wang, Y.Q., 2014. MeteoInfo: GIS software for meteorological data visualization and
 1109 analysis. *Meteorological Applications* 21, 360–368.
 1110 <https://doi.org/10.1002/met.1345>
 1111 Wang, Y.Q., Zhang, X.Y., Draxler, R.R., 2009. TrajStat: GIS-based software that uses
 1112 various trajectory statistical analysis methods to identify potential sources from
 1113 long-term air pollution measurement data. *Environmental Modelling &*
 1114 *Software* 24, 938–939. <https://doi.org/10.1016/j.envsoft.2009.01.004>
 1115 WHO global air quality guidelines: Particulate matter (PM_{2.5} and PM₁₀), ozone,
 1116 nitrogen dioxide, sulfur dioxide and carbon monoxide, 2021. , WHO Guidelines
 1117 Approved by the Guidelines Review Committee. World Health Organization,
 1118 Geneva.
 1119 Xie, C., He, Y., Lei, L., Zhou, W., Liu, J., Wang, Q., Xu, W., Qiu, Y., Zhao, J., Sun, J.,
 1120 Li, L., Li, M., Zhou, Z., Fu, P., Wang, Z., Sun, Y., 2020. Contrasting mixing
 1121 state of black carbon-containing particles in summer and winter in Beijing.
 1122 *Environmental Pollution* 263, 114455.
 1123 <https://doi.org/10.1016/j.envpol.2020.114455>
 1124 Xu, J., Ge, X., Zhang, X., Zhao, W., Zhang, R., Zhang, Y., 2020. COVID-19 Impact on
 1125 the Concentration and Composition of Submicron Particulate Matter in a
 1126 Typical City of Northwest China. *Geophysical Research Letters* 47,
 1127 e2020GL089035. <https://doi.org/10.1029/2020GL089035>
 1128 Yang, J., Ma, S., Gao, B., Li, X., Zhang, Y., Cai, J., Li, M., Yao, L., Huang, B., Zheng,
 1129 M., 2017. Single particle mass spectral signatures from vehicle exhaust particles
 1130 and the source apportionment of on-line PM_{2.5} by single particle aerosol mass
 1131 spectrometry. *Science of The Total Environment* 593–594, 310–318.
 1132 <https://doi.org/10.1016/j.scitotenv.2017.03.099>
 1133 Zhang, G., Fu, Y., Peng, X., Sun, W., Shi, Z., Song, W., Hu, W., Chen, D., Lian, X., Li,
 1134 L., Tang, M., Wang, X., Bi, X., 2021. Black Carbon Involved Photochemistry
 1135 Enhances the Formation of Sulfate in the Ambient Atmosphere: Evidence From
 1136 In Situ Individual Particle Investigation. *Geophys Res Atmos* 126.
 1137 <https://doi.org/10.1029/2021JD035226>
 1138 Zhang, J., Li, H., Chen, L., Huang, X., Zhang, W., Zhao, R., 2022. Particle composition,
 1139 sources and evolution during the COVID-19 lockdown period in Chengdu,
 1140 southwest China: Insights from single particle aerosol mass spectrometer data.
 1141 *Atmospheric Environment* 268, 118844.
 1142 <https://doi.org/10.1016/j.atmosenv.2021.118844>
 1143 Zhang, J., Yuan, Q., Liu, L., Wang, Y., Zhang, Y., Xu, L., Pang, Y., Zhu, Y., Niu, H.,
 1144 Shao, L., Yang, S., Liu, H., Pan, X., Shi, Z., Hu, M., Fu, P., Li, W., 2021. Trans-
 1145 Regional Transport of Haze Particles From the North China Plain to Yangtze
 1146 River Delta During Winter. *JGR Atmospheres* 126.

1147 <https://doi.org/10.1029/2020JD033778>

1148 Zhang, K., Liu, Z., Zhang, X., Li, Q., Jensen, A., Tan, W., Huang, L., Wang, Y., de Gouw,
1149 J., Li, L., 2022. Insights into the significant increase in ozone during COVID-
1150 19 in a typical urban city of China. *Atmos. Chem. Phys.* 22, 4853–4866.
1151 <https://doi.org/10.5194/acp-22-4853-2022>

1152 Zhang, Y., Liu, X., Zhang, L., Tang, A., Goulding, K., Collett, J.L., 2021. Evolution of
1153 secondary inorganic aerosols amidst improving PM2.5 air quality in the North
1154 China plain. *Environmental Pollution* 281, 117027.
1155 <https://doi.org/10.1016/j.envpol.2021.117027>

1156 Zhang Y., Wang X., Chen H., Yang X., Chen J., Alien J.O., 2009. Source Apportionment
1157 Of Lead-containing Aerosol Particles In Shanghai Using Single Particle Mass
1158 Spectrometry. *Chemosphere* 74, 501–507.

1159 Zhang, Y., Yuan, Q., Huang, D., Kong, S., Zhang, J., Wang, X., Lu, C., Shi, Z., Zhang,
1160 X., Sun, Y., Wang, Z., Shao, L., Zhu, J., Li, W., 2018. Direct Observations of
1161 Fine Primary Particles From Residential Coal Burning: Insights Into Their
1162 Morphology, Composition, and Hygroscopicity. *Journal of Geophysical*
1163 *Research: Atmospheres* 123, 12,964–12,979.
1164 <https://doi.org/10.1029/2018JD028988>

1165 Zhang, Z., Li, H., Ho, W., Cui, L., Men, Q., Cao, L., Zhang, Y., Wang, J., Huang, C.,
1166 Lee, S., Huang, Y., Chen, M., Ge, X., 2024. Critical Roles of Surface-Enhanced
1167 Heterogeneous Oxidation of SO₂ in Haze Chemistry: Review of Extended
1168 Pathways for Complex Air Pollution. *Curr Pollution Rep.*
1169 <https://doi.org/10.1007/s40726-023-00287-2>

1170 Zhou, H., Liu, T., Sun, B., Tian, Y., Zhou, X., Hao, F., Chun, X., Wan, Z., Liu, P., Wang,
1171 J., Du, D., 2022. Chemical characteristics and sources of PM_{2.5} in Hohhot, a
1172 semi-arid city in northern China: insight from the COVID-19 lockdown. *Atmos.*
1173 *Chem. Phys.* 14.

1174 Zhou, X., Gao, J., Wang, T., Wu, W., Wang, W., 2009. Measurement of black carbon
1175 aerosols near two Chinese megacities and the implications for improving
1176 emission inventories. *Atmospheric Environment* 43, 3918–3924.
1177 <https://doi.org/10.1016/j.atmosenv.2009.04.062>

1178 Zhou, Y., Wu, Y., Yang, L., Fu, L., He, K., Wang, S., Hao, J., Chen, J., Li, C., 2010. The
1179 impact of transportation control measures on emission reductions during the
1180 2008 Olympic Games in Beijing, China. *Atmospheric Environment* 44, 285–
1181 293. <https://doi.org/10.1016/j.atmosenv.2009.10.040>

1182 Zhu, X., Hu, B., Xin, J., Wang, L., Munkel, C., Mao, G., Wang, Y., 2015. Impact of
1183 emission controls on air quality in Beijing during APEC 2014: Lidar ceilometer
1184 observations. *ATMOSPHERIC CHEMISTRY AND PHYSICS* 15, 12667–
1185 12680. <https://doi.org/10.5194/acp-15-12667-2015>

带格式的: 缩进: 左侧: 0 厘米, 悬挂缩进: 7.2 字符, 不允许文字在单词中间换行